Journal of Alloys and Compounds 1062 (2026) 187401

Contents lists available at ScienceDirect

Journal of Alloys and Compounds

journal homepage: www.elsevier.com/locate/jalcom

Characterization of the as-cast microstructure, precipitates stability and corrosion resistance of Alloy 718 modified with ex-situ WC nanoparticles

Łukasz Rakoczy [a,*], Małgorzata Grudzień-Rakoczy [b], Rafał Cygan [c,d], Grzegorz Cios [e], Tomasz Dudziak [b], Norbert Schell [f], Tomasz Kargul [a], Marcin Madej [a], Grzegorz Cempura [a], Ewa Rząd [b], Dawid Kozień [g], Robert Chulist [a], Shigenari Hayashi [h]

[a] AGH University of Kraków, Faculty of Metals Engineering and Industrial Computer Science, al. Mickiewicza 30, Kraków 30-059, Poland
[b] Łukasiewicz Research Network-Kraków Institute of Technology, ul. Zakopiańska 73, Kraków 30-418, Poland
[c] AGH University of Kraków, Faculty of Foundry Engineering, Władysława Reymonta 23, Kraków 30-059, Poland
[d] Consolidated Precision Products, ul. Hetmańska 120, Rzeszów 35-078, Poland
[e] AGH University of Kraków, Academic Centre for Materials and Nanotechnology, al. Mickiewicza 30, Kraków 30-059, Poland
[f] Institute of Materials Physics, Helmholtz-Zentrum Hereon, Max-Planck-Strasse 1, Geesthacht 21502, Germany
[g] AGH University of Kraków, Faculty of Materials Science and Ceramics, al. Mickiewicza 30, Kraków 30-059, Poland
[h] Hokkaido University, Faculty of Engineering, N13, W8, Kitaku, Sapporo 060-8628, Japan

ARTICLE INFO

Keywords:
MMC
Tungsten carbide
718
Inconel
Superalloy

ABSTRACT

The extension of service life of Ni-based superalloys requires repair materials capable of operating in wear and corrosive environments, where conventional filler alloys often lack sufficient robustness. This work evaluates Alloy 718 reinforced with WC nanoparticles as candidates for such applications. Ex-situ composites containing 1.25–5.0% WC were produced by suction casting, and their microstructure, phase composition, tribological and corrosion behavior were characterized. A dendritic structure consisting of a γ-matrix was observed in all variants. In the unreinforced alloy, segregation to interdendritic regions led to precipitation (Nb,Mo)C carbides and Laves phase. Synchrotron-based analyses, coupled with electron microscopy, confirmed partial dissolution of WC during solidification, leading to complex (Nb,Mo,W)C carbides and a marked reduction in the Laves phase. Steam oxidation at 704 °C for 1000 h showed that all WC-modified variants exhibited lower mass gain compared with Alloy 718. Exposure in Ar+ 0.25% SO_2 revealed that increasing WC content suppressed Ni_3S_2 formation and reduced mass gain to 1.144 mg·cm^{-2} at 5% WC. Hardness increased from 198HV10 to 221HV10 with 5% WC, accompanied by a modest improvement in dry-sliding wear resistance. These results demonstrate that WC-reinforced Alloy 718 offer enhanced environmental resistance and improved mechanical response, making them promising repair materials for Ni-based superalloys.

1. Introduction

Ni-based superalloys are indispensable materials in aerospace, power generation, and petrochemical industries due to their excellent strength, oxidation resistance, and phase stability at elevated temperatures [1]. Components manufactured from these alloys, particularly turbine blades, vanes, shrouds, and combustor hardware, operate in environments characterized by steep thermal gradients, cyclic mechanical loading, particulate erosion, and corrosive atmospheres [2]. These demanding conditions inevitably lead to degradation mechanisms, including tip wear, hot corrosion, sulfidation, microcracking, and foreign-object damage. From an industrial perspective, extending the lifespans of such high-value components is not only technologically desirable but also economically imperative for sustainability, circular manufacturing, and life-cycle cost reduction. Consequently, selecting filler materials with specific properties-such as high weldability, crack resistance, and thermal compatibility-is essential for successful repair [3]. Recent findings indicate that the stress field at the squealer tip is relatively low, suggesting that modern Ni-based superalloys may not be necessary there [4]. Kang et al. [5] calculated that the stress near the blade root for root and tip radii of 0.55 m and 0.53 m is roughly 61 MPa. Precipitation-strengthened Ni-based superalloys often exhibit a high

* Corresponding author.
E-mail address: lrakoczy@agh.edu.pl (Ł. Rakoczy).

https://doi.org/10.1016/j.jallcom.2026.187401
Received 8 February 2026; Received in revised form 5 March 2026; Accepted 15 March 2026
Available online 17 March 2026

fraction of γ′ phase, which, while beneficial for creep resistance, increases susceptibility to liquation and solidification cracking during fusion-based repair processes [6]. Alloys that exhibit high weldability and comparatively lower fractions of strengthening precipitates are therefore preferred as repair fillers, with Alloy 718 (Inconel 718) being widely recognized for this purpose due to its favorable combination of weldability, corrosion resistance, and service strength up to approximately 650 °C. However, despite these advantages, conventional Alloy 718 still exhibits insufficient hardness and wear resistance in applications involving intense abrasion or impact at elevated temperatures, conditions typically experienced by blade tips and seal segments [7].

This performance limitation has catalyzed interest in Ni-alloy-based metal matrix composites (MMCs). In these systems, ceramic reinforcements are added to enhance wear and corrosion resistance, as well as high-temperature strength. Ceramic particles such as carbides (TiC [8], NbC [9]), oxides (Al_2O_3 [10], Y_2O_3 [11]), and borides (TiB_2 [12]) have been incorporated into various Ni-based matrices. These efforts have shown improvements in hardness and tribological behavior. Among the reinforcing phases, tungsten carbide (WC) is particularly attractive due to its exceptional hardness of nearly 26 GPa and fracture toughness (~5.9 MPa·$m^{1/2}$). It also offers moderate thermal conductivity (~130 W/m·· K), outstanding wear resistance, and good mechanical strength up to 1000 °C [13]. Its high melting point (2870 °C) and stiffness make it suitable for severe-service applications where conventional Ni-alloys degrade rapidly. Tungsten carbides exhibit favorable wettability and chemical compatibility with metallic matrices, mainly due to their relatively low thermal expansion. This enhances confidence in their bonding and overall performance. WC has a hexagonal crystal structure (a = b = 2.9290 Å, c = 2.8400 Å), whereas γ-Ni has a cubic structure (a=b=c=3.4800 Å). The lattice mismatch between WC and γ-Ni, which lies between 6% and 12%, allows WC to act as a highly effective nucleation site for γ-Ni [14]. This limited interfacial disregistry helps develop semi-coherent interfaces. As a result, WC is widely recognized as a promising reinforcement for Ni-based alloys by enhancing interfacial bonding and stabilizing the matrix through controlled interfacial reactions [15].

Previous studies on Ni-based alloy+WC systems have demonstrated that WC forms effective metallurgical bonding with Alloy 718, providing nucleation sites that increase both hardness and wear resistance [16–18]. According to Lu Xu et al. [19], who laser-cladded IN718 composite coatings with different WC–Co particle sizes and concentrations, increasing WC–Co addition led to the simultaneous formation of various carbides, pronounced grain refinement, and superior hardness and wear resistance, accompanied by an increased tendency toward cracking. Deschuyteneer et al. [20] reported that NiCrBSi/WC coatings produced by laser cladding exhibited contrasting behavior depending on the carbide morphology. Coarse WC promoted superior wear resistance under rolling contact, whereas finer carbides were more beneficial in sliding wear regimes. García et al. [21] further showed that the improvement in wear resistance is strongly dependent on WC content. The wear rate decreases rapidly with increasing reinforcement fraction up to approximately 27 wt%, beyond which additional WC produces only marginal benefits. Increasing WC levels also alters the dominant wear mechanisms, leading to a transition from adhesive/oxidative to predominantly abrasive wear. Paul et al. [22] investigated Ni+WC composite clads fabricated by laser cladding, focusing on solid particle erosion. The study indicated that greater WC additions were associated with improved hardness and superior erosion resistance. Investigations by Tian et al. [23] on multilayer Inconel 625/WC claddings revealed an important trade-off, although higher WC contents enhance wear performance, they may simultaneously deteriorate corrosion resistance. Consequently, corrosion behavior must be assessed alongside tribological evaluation, particularly given the service environment. Liu et al. [24] showed that, for HVOF-sprayed coatings, the decline in corrosion resistance arises mainly from partial dissolution of WC and the associated formation of secondary carbides.

Yet, achieving the desired synergy between the metallic matrix and ceramic reinforcement remains far from trivial. The beneficial effect of WC additions depends strongly on processing route, interfacial reactions, particle stability, degree of dissolution, and spatial distribution within the matrix. Partial dissolution of WC during high-temperature processing can release W and C into the melt. This release promotes the formation of secondary carbides or complex intermetallics. Microstructural changes induced by its dissolution represent key challenges limiting the reliable use of Ni-based alloy/WC composites in harsh operating environments [25]. Such changes may either strengthen or provoke embrittlement and corrosion susceptibility, depending on the resulting chemistry and morphology. Moreover, the large density difference between WC (15.63 g/cm^3) and Ni-based superalloys (8.19–8.22 gm/cm^3 for Alloy 718) can promote particle segregation, agglomeration, or sedimentation. This difference can lead to local compositional heterogeneity and nonuniform mechanical response [26]. Understanding and controlling these phenomena requires a detailed analysis of the as-cast microstructure and early-stage phase stability of the composite system. Another crucial aspect is corrosion behavior because repaired components frequently operate in oxidizing or sulfur-containing environments at intermediate to high temperatures. The incorporation of WC can influence passivation kinetics, change local galvanic interactions, and modify diffusion pathways at grain boundaries [27]. Secondary carbides or W-rich phases formed via WC dissolution may either stabilize or destabilize the passive film, depending on the extent of microstructural degradation [28]. Hence, any new composite filler material intended for the repair of Ni-based superalloys must be evaluated not only in terms of hardness or wear behavior but also for corrosion resistance, which is directly linked to service durability. Among various fabrication routes, suction casting presents a compelling method for producing small-diameter rods and laboratory-scale billets for welding or cladding applications. The rapid solidification inherent to suction casting can refine dendritic structures, suppress porosity, and reduce segregation compared with conventional casting. These features are beneficial for fabricating composite filler rods, where microstructural uniformity and low defect content are essential for stable deposition during repair.

Existing studies on Ni-based alloy + WC systems primarily focus on performance improvements, such as hardness and wear resistance. At the same time, the underlying mechanisms of phase evolution and carbide transformation remain unclear. There is consensus that WC additions can enhance tribological performance. However, significant discrepancies remain regarding the stability of WC particles and the extent of their dissolution during high-temperature processing. In particular, the interaction between dissolved W and C and the formation of MC carbides in Nb-containing superalloys, such as Alloy 718, has not yet been systematically elucidated. Furthermore, most previous research has focused on coatings produced by laser cladding or thermal spraying. The microstructure and properties of WC-modified Alloy 718 processed under suction-casting conditions remain insufficiently explored, particularly with respect to WC dissolution kinetics and their combined impact on wear and corrosion performance. The current research addresses this knowledge gap by investigating the relationship among processing, microstructure, and properties. It first focuses on the evolution of the as-cast microstructure of WC-modified Alloy 718, including phase transformation temperatures, phase composition, and, finally, the resulting tribological and corrosion behavior. In a broader sense, the work advances repair and remanufacturing technologies for Ni-based superalloys, consistent with industrial trends toward sustainability, resource efficiency, and extended component life.

2. Materials and methodology

2.1. Fabrication of materials

The Alloy 718 atomised powder (Ni-19.8Cr-18.55Fe-5.2Nb-2.98Mo-

0.56Al-0.1Si-0.005 C, wt%) with a spherical particle size distribution of 20–45 μm served as the matrix of the composite. As the ex-situ reinforcing phase, tungsten carbides (NPs- nanoparticles) with a purity of 99.5% and an average particle size below 100 nm were employed. Subsequently, they were blended in the Fritsch Pulverisette 6 planetary mill to homogenize Alloy 718 with WC (+1.25, 2.5, 3.75, and 5.0%). Each variant served as the feedstock for fabricating cylindrical rods (φ5 ×50 mm) via suction casting with an arc-melting system (Edmund Bühler GmbH). The assembly comprised a water-cooled copper base and a two-part mold, which enabled rapid suction of the liquid material into the mold's cavity. The protective atmosphere was achieved using Ar (5.0) via three successive cycles of evacuation and backfilling, while a titanium getter was used to remove residual oxygen. Melting of powders was carried out using an electric arc generated between a tungsten electrode and a copper base. Upon opening the drain valve, the molten material was rapidly drawn into the mold due to the pressure gradient between the chamber and the vacuum reservoir. Suction-cast rods with a 5 mm diameter exhibit cooling rates of about 100 °C/s [29]. It leads to solidification within a few seconds. Both ends of the cast rods were machined, and the resultant specimens were prepared for the subsequent characterization procedures described in the following section.

2.2. Methodology of experiments

2.2.1. Thermodynamical modelling with Thermo-Calc® software

Thermodynamic simulations were performed with Thermo-Calc® software (TCNI:10 database, 2024b) to assess phase stability and solidification for tungsten and carbon enrichment. The simulations assumed complete dissolution of WC particles in the Alloy 718 matrix. The Scheil–Gulliver approximation was used to model non-equilibrium solidification, identifying both primary solidification phases and segregation tendencies. Equilibrium calculations complemented this by determining the stability ranges of secondary phases over 600–1400 °C.

2.2.2. Dilatometry and differential scanning calorimetry

Thermal expansion behavior was investigated using a non-contact optical dilatometer (TA Instruments DIL 806). This instrument measures changes in the length of a sample without physical contact as it is heated. Cylindrical specimens (φ4.5 mm×20 mm), were heated from room temperature to 1240 °C at a steady rate of 0.08 °C/s. The measured change in sample length at different temperatures was used to determine the linear coefficient of thermal expansion (CTE). Differential scanning calorimetry (DSC) was performed with a Netzsch STA 449F3 Jupiter thermal analyzer. In this method, about 0.1 g of material was placed in covered crucibles made of aluminum oxide (Al_2O_3). The DSC involves controlled heating from room temperature to 1400 °C at 20 °C/min, holding the sample at 1400 °C for 3 min to allow the temperature to stabilize, and then cooling to 1000 °C at the same rate.

2.2.3. High-energy synchrotron X-ray diffraction

Phase identification and quantitative phase analysis were performed at room temperature using high-energy synchrotron X-ray diffraction at the PETRA III facility (DESY, Hamburg, Germany). Polished disc-shaped specimens (φ5 × 2 mm) were examined using monochromatic radiation (λ = 0.142342 Å). Two-dimensional diffraction data were processed using the Fit2D software. To improve statistical reliability and achieve accurate Rietveld refinement, samples were continuously rotated by 90° around the ω-axis during data acquisition, enabling the collection of complete diffraction rings within a single detector exposure, thereby improving the precision of volume fraction measurements [30,31].

2.2.4. Scanning- and scanning-transmission electron microscopy

Suction-cast rods for SEM analysis were cut into slides, mechanically ground with SiC papers, and polished with diamond suspensions, followed by final polishing with OP-S colloidal silica. Electrochemical etching was performed in a 10% oxalic acid solution for 5 s to reveal microstructural features. Observations were conducted using a Thermo Fisher Scientific Phenom XL microscope equipped with an Energy-Dispersive X-ray spectroscopy (EDX) detector, operated at an accelerating voltage of 20 kV. Distribution maps were acquired to assess solute partitioning. The partitioning coefficient k^i for individual alloying elements was calculated using Eq. (1):

$$k^i = \frac{C_D^i}{C_0^i} \tag{1}$$

Where: C_D^icorresponds to the concentration of element measured in dendrite cores via point analysis, and C_0^i represents the average concentration in region encompassing both dendritic and interdendritic areas, at.%

The crystallographic orientation of the microstructural regions was determined by electron backscatter diffraction (EBSD). Measurements were performed using a field-emission scanning electron microscope (FE-SEM, FEI VERSA 3D) equipped with an Oxford Instruments Symmetry S2 CMOS EBSD detector, enabling the acquisition of diffraction patterns and the generation of crystallographic orientation maps. EBSD data were acquired at an accelerating voltage of 20 kV, a probe current of approximately 26 nA, and a specimen tilt angle of 70°, using a step size of 100 nm. Diffraction patterns were stored and subsequently reprocessed using dynamic template matching implemented in AZtec Crystal MapSweeper software. This approach was employed to overcome limitations of conventional Hough-based indexing in distinguishing crystallographically similar phases, thereby improving phase discrimination between NbC precipitates and the FCC matrix and enhancing the reliability of Laves-phase indexing.

The Alloy 718 + 5.0 wt% WC variant was selected as a representative material for scanning-transmission electron microscopy (STEM). Electron-transparent lamellae were prepared from targeted regions using Ga^+ focused ion beam milling in a Zeiss Crossbeam 350 system. STEM investigations were performed using a Cs-corrected FEI Titan Cubed G2 60–300 microscope operating at 300 kV and equipped with a ChemiSTEM detector system. Imaging was conducted in bright-field TEM and high-angle annular dark-field (STEM-HAADF) modes. Crystallographic and phase identification analyses were performed using selected area electron diffraction (SAED) and atomic-resolution imaging, with fast Fourier transform (FFT) analysis indexed using JEMS software.

2.2.5. Oxidation resistance tests in steam and Ar+ 0.25% SO2 gas mixture

The oxidation behaviour of the materials was evaluated using disc-shaped specimens (φ5 × 2 mm) that were ground on sandpaper (final grit size 2000) and then ultrasonically cleaned in isopropanol in an ultrasonic bath for 15 min at 40 °C. After drying, the specimens have been carefully weighed using an analytical balance (accuracy 10^{-5} g). Steam oxidation tests were conducted at 704 °C in a steam with an oxygen partial pressure of 10^{-8} under a total pressure of 0.1 MPa, following procedures described in Ref. [32]. High-temperature corrosion experiments in a more aggressive environment were carried out at 704 °C in an Ar + 0.25 vol% SO_2 gas mixture, creating a reduced-oxygen environment. The experimental setup and exposure protocol followed methodologies reported elsewhere [33]. Mass gain measurements in both tests were recorded after exposure durations of 10, 25, 100, 250, 500, 750, and 1000 h. Oxidation kinetics were evaluated using the time exponent approach according to Eq. (2):

$$\log\left(\frac{\Delta W}{A}\right) = \log k + \quad n\log t \tag{2}$$

Where: ΔW is the mass change, mg; A is the exposed surface area, cm^2; k is the rate constant, t is time, h; and n is the kinetic exponent.

After 1000 h of exposure, the surface and cross-sectional morphologies of the oxide scales were examined by SEM. Phase identification of

the corrosion products was performed by X-ray diffraction using a Panalytical Empyrean diffractometer equipped with CuKα radiation (λ = 1.5405 Å) and X'Pert HighScore software.

2.2.6. Hardness and wear resistance tests

Vickers hardness (10 kgf) measurements were performed using a Zwick/Roell hardness tester. For each material variant, 10 indentations were made to obtain statistically representative average hardness values and standard deviations. Dry-sliding wear resistance was evaluated using a T-05 roller block tribometer in accordance with the requirement of ASTM G77 standard [34]. Rectangular specimens (4 × 4 × 20 mm) were tested against a hardened 100Cr6 steel ring (55 HRC, φ49.5 × 8 mm). The contact surfaces of the countersamples were prepared by grinding and polishing to obtain an average surface roughness of R_a= 0.3 μm. The tribological tests were carried out under controlled laboratory conditions at 21 °C and 43% relative humidity. The test configuration ensured perpendicular contact between the specimen and the rotating counterpart. Testing parameters included a rotational speed of 200 rpm, an applied load of 100 N, and a sliding distance of 500 m. Wear rates were calculated using Eq. (3):

$$W_r = \frac{\Delta m}{L \cdot Sd} \quad (3)$$

where Δm is the mass loss, mg; L is the applied load, N; $S_d$is the sliding distance.

Post-test wear surfaces were analyzed using SEM in both secondary electron (SE) and backscattered electron (BSE) imaging modes to elucidate dominant wear mechanisms.

3. Results and discussion

3.1. Scheil solidification modeling and equilibrium phase stability predicted by Thermo-Calc

In the ThermoCalc modelling, it is assumed that the ex-situ-introduced WC nanoparticles completely dissolve during suction casting, resulting in local enrichment of Alloy 718 with W and C. The Scheil solidification simulations, together with equilibrium phase stability predictions, indicate how dissolution of WC may modify the alloy's solidification path and phase stability (Table 1, Fig. 1). For the reference Alloy 718, the model predicts solidification to start with the formation of a Ni-rich γ matrix, followed by precipitation of MC-type carbides and the Laves (C14) phase. Owing to compositional segregation, the intermetallic δ-Ni_3Nb (D0a) phase may also form. However, its formation requires pronounced segregation and extended time, conditions more typical of large industrial castings than of rapidly solidified suction-cast rods. When the alloy composition is enriched in W and C, corresponding to additions of 1.25% WC and 2.5% WC, the simulations forecast the same principal phases: γ matrix, Laves phase, MC carbide, and the possible appearance of the δ phase. Notably, the δ phase is not predicted to form in the 3.75% and 5.0% WC-containing variants, implying that Nb is preferentially tied up through MC carbide formation due to the additional carbon supplied by dissolved WC. This suggests that partial dissolution of WC NPs is more likely to promote the reprecipitation of complex MC carbides rather than the regeneration of stoichiometric WC.

Equilibrium phase fraction vs temperature diagrams for the Alloy 718 and for its compositions enriched in W and C are shown in Fig. 1. The simulations for the reference alloy predict the presence of δ and γ′ intermetallic phases together with MC and $M_{23}C_6$ carbides. In heat-treated Alloy 718, γ′ and γ″ precipitates are the key strengthening constituents. They typically occur as nanoscale particles within the γ matrix and maintain coherent or semi-coherent interfaces with it [35]. The γ″ phase is metastable and may transform into δ during extended ageing, a transformation pathway that is also reflected in the simulation results. The calculated phase stability limits indicate that γ′ persists up to approximately 781 °C, while δ remains stable up to about 1034 °C. MC carbides exhibit a high solvus temperature, close to 1184 °C, and therefore tend to coexist with the γ matrix throughout solution treatment. Below roughly 736 °C, $M_{23}C_6$ carbides become thermodynamically favoured through the reaction MC + γ → $M_{23}C_6$ + γ′. Enrichment in W and C associated with dissolution of WC NPs markedly modifies the stability ranges and relative fractions of these phases in the Alloy 718 matrix. In Alloy 718 and the modified variants, the model predicts that under equilibrium conditions, the main strengthening phase is δ-Ni_3Nb, which is a stable phase formed from the phase transformation of metastable γ"-Ni_3Nb precipitates. However, modification of the chemical composition decreases its stability, and the solvus temperature of the δ phase drops to approximately 900°C in the Alloy 718 + 5.0% WC variant. A similar trend is also evident in the δ-phase volume fractions determined at 704°C across variants. Due to the presence of Al and Ti in the chemical composition of Alloy 718, the model predicts the presence of the intermetallic γ' phase under equilibrium conditions. As in the case of the δ phase, a decrease in the γ' solvus temperature is observed with chemical composition modification from 780°C to 730°C. The Scheil model did not predict the γ' intermetallic phase because it precipitates from the supersaturated γ solution after the material has solidified. The Scheil solidification model predicted that the main primary strengthening phase is MC carbides, which is known for its very high stability at high temperatures, as shown in the graph under equilibrium conditions. The solvus temperature of the MC carbides increases with the initial amounts of W and C in Alloy 718, thus, in the Alloy 718 + 5.0% WC variant, it dissolves in the liquid above 1400 °C. At intermediate temperatures, the model predicts that $M_{23}C_6$ carbides will be more stable. This behaviour indicates a potential MC+ γ→$M_{23}C_6$+ γ' phase transformation. However, this transformation occurs very slowly, and even after long service, MC carbides remain in the microstructure. The scale of this phase transformation is illustrated by the example of the heat-treated René 108 Ni-based superalloy casting [36]. Ageing led to the formation of a 10 nm-thick $M_{23}C_6$ layer via phase transformation. Similarly, such a transformation can occur during the service of Alloy 718 +WC. The solvus temperature of $M_{23}C_6$ carbides does not change significantly with increasing W and C concentrations in the Alloy 718, probably because the main carbide-forming element in the crystal

Table 1
Summary of Scheil solidification results (primary phases), transformation temperatures, and equilibrium phase fractions at 704 °C for Alloy 718 and variants with W and C.

Addition of WC to Alloy 718, %wt	0	1.25	2.5	3.75	5.0
	Phases and phase transformation temperature predicted by Scheil solidification modelling				
Phase	γ, Laves, MC, δ	γ, Laves, MC, δ	γ, Laves, MC, δ	γ, Laves, MC	γ, Laves, MC
Solidus/ Liquidus	1252/ 1336	1261/ 1331	1269/ 1327	1280/ 1327	1287/ 1330
	Solvus temperature of phase in equilibrium conditions, °C				
$M_{23}C_6$	736	739	728	729	733
Laves	-	631	739	820	890
δ	1000	980	948	929	900
γ'	780	761	751	740	730
MC	1185	1300	1320	1390	< 1400
	Volume fraction of phase in 704°C in equilibrium conditions				
$M_{23}C_6$	0.0009	0.0206	0.0405	0.0595	0.0654
Laves	0	0	0.0054	0.0177	0.0324
δ	0.161	0.162	0.160	0.157	0.152
γ'	0.0246	0.0254	0.0243	0.0264	0.0218
MC	0	0	0	0	
	Solidus-liquidus temperature range in equilibrium conditions, °C				
Solidus	1259	1270	1279	1280	1290
Liquidus	1329	1329	1325	1320	1319

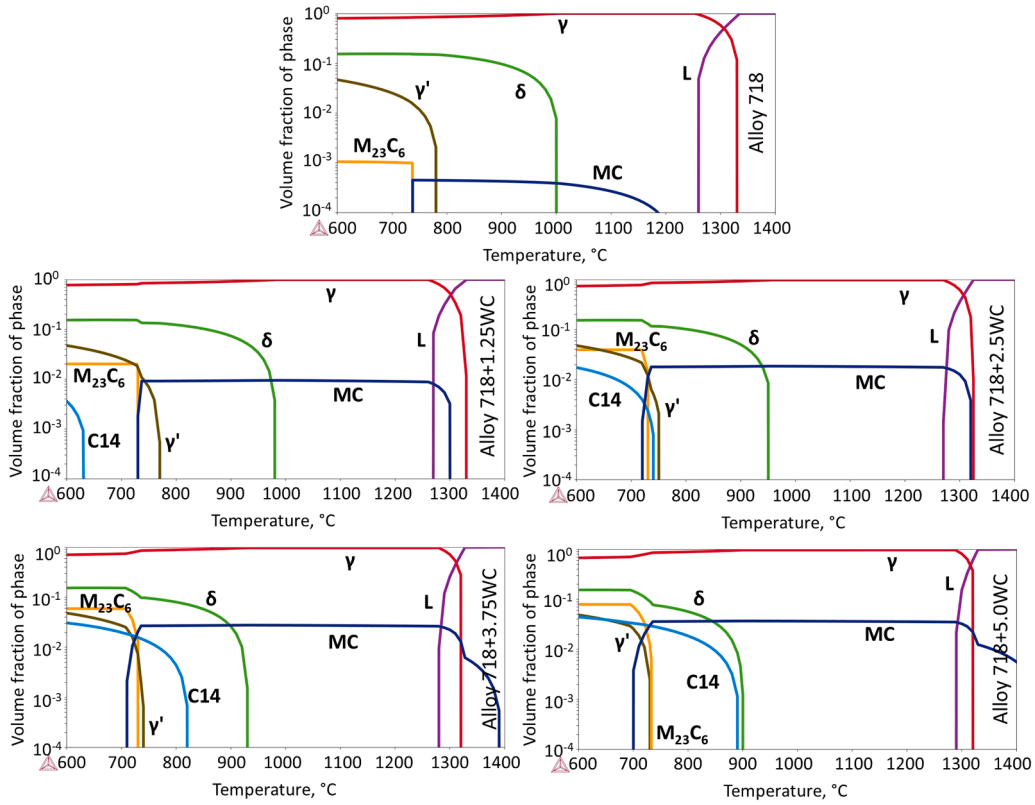

Fig. 1. Equilibrium phase stability of Alloy 718 and W- and C-modified compositions.

structure is Cr. It can only be seen that increasing C concentration causes it to theoretically be bound by Cr from the γ solid solution at intermediate temperatures, which translates into an increase in the volume fraction at 704 °C from 0.0009 in the Alloy 718 superalloy to 0.0654 in the Alloy 718 + 5.0% WC variant. Because the model predicts the transformation of the Nb-rich MC carbide into a carbide composed primarily of Cr, the excess Nb is bound by Ni to the Laves phase. Therefore, the phase equilibrium diagram shows an increase in the volume fraction of this phase with increasing W and C concentrations. Because of their pronounced thermodynamic stability, MC carbides are expected to make an important contribution to strengthening at both room and elevated temperatures. The simulations further show that the solidus temperature rises from about 1270 °C (+1.25% WC) to approximately 1290 °C as the WC content increases to 5.0%. In contrast, the liquidus temperature decreases slightly with increasing W and C additions, from 1329 °C to 1319 °C. These trends indicate that the dissolution of WC NPs into Alloy 718 can modify its solidification behaviour and, consequently, its microstructure and properties. This observation forms the basis for the experimental investigations discussed in the following subsections.

The DSC heating curves of the reference Alloy 718 and the four WC-modified variants, along with corresponding data on phase transformation temperatures, are presented in Fig. 2 and Table 2. A sequence of closely spaced endothermic effects is observed between 1150 and 1275 °C during heating of the unmodified Alloy 718. These endothermic effects are interpreted as manifestations of incipient melting occurring ahead of the principal melting peak. The first peak in the sequence, observed at around 1186 °C, is assigned to the dissolution of the Laves phase. Comparable endothermic effect between 1162 °C and 1190 °C was reported in as-cast Alloy 718 [37], linking it to a Laves/γ eutectic reaction. After melting begins, the degree of liquation rises sharply with temperature. Sohrabi et al. [38] observed that, during annealing of Inconel 718, the Laves phase begins to dissolve at temperatures slightly above 1150 °C and disappears as the temperature approaches 1200 °C. This evidence strongly supports attributing the initial DSC endothermic

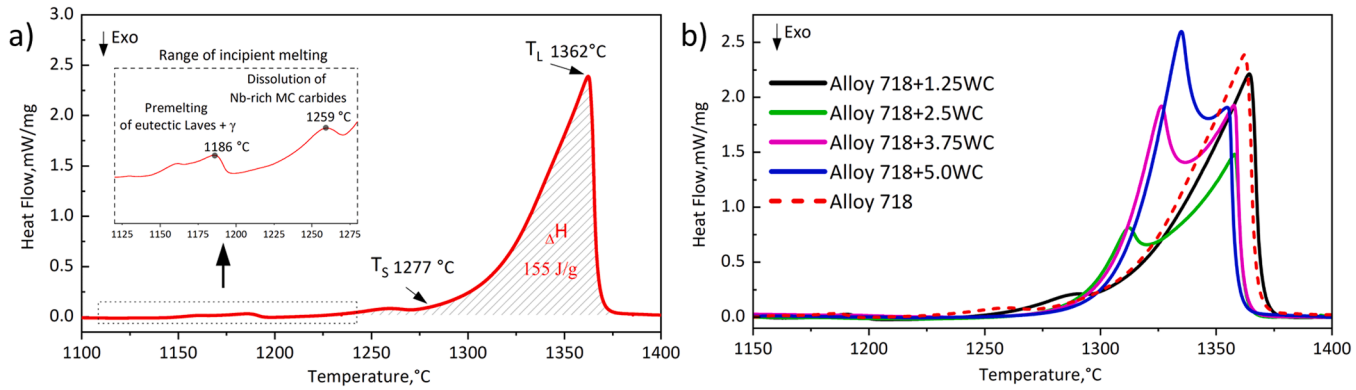

Fig. 2. DSC on-heating thermograms obtained for: a) Alloy 718; b) Alloy 718 with WC.

Table 2
DSC-determined phase transformation temperatures of Alloy 718 + WC nanocomposites.

WC addition to Alloy 718, °C	0	1.25	2.5	3.75	5
Upon Heating at 20 °C/min					
Max. rate of Laves phase dissolution, °C	1186	1190	1182	1195	1206
Max. rate of carbides dissolution, °C	1259	1288	1312	1326	1335
Solidus	1277	1273	1277	1267	1276
Liquidus, °C	1362	1364	1358	1358	1354
Upon cooling at 20 °C/min					
Liquidus, °C	1344	1315	1309	1302	1308
Solidus, °C	1256	1257	1257	1256	1258
Max. rate of carbides/ Laves phase precipitation, °C	- /1156	1252/ 1072	1283/ 1089	1289/ 1109	1296/ 1129

signals to Laves-phase dissolution. The next endothermic peak, centered near 1259 °C, is likely related to NbC carbides dissolution and exhibits a lower intensity, implying a reduced phase fraction. The extrapolated onset of melting (Solidus) was found at 1277 °C, while the liquidus temperature is recorded at 1362 °C. Accordingly, the melting range of the reference Alloy 718 is about 85 °C. The total melting enthalpy, evaluated by integrating the area under all discernible endothermic peaks, is approximately 155 J/g. The DSC heating curve of the Alloy 718 + 1.25% WC composite exhibits a shape and endothermic features very similar to those of the reference variant. The first endothermic effect, observed at 1190 °C, is most likely associated with the dissolution of the intermetallic Laves phase. The addition of 1.25% WC therefore slightly raises the solvus temperature of the Laves phase, however, the reduced intensity of this effect suggests its lower initial volume fraction. Further support for this interpretation is provided by the more pronounced endothermic peak detected at 1288 °C, which is attributed to the dissolution of MC carbides. Notably, this solvus temperature is 29 °C higher than that of the reference alloy, indicating a modification of the carbides' chemical composition. Further increasing the WC content in Alloy 718 results in pronounced changes in the shape of the DSC curve. Within the temperature range of 1125–1225 °C, only very small endothermic effects attributable to the dissolution of the Laves phase are detected. Compared with the two previously analysed samples, this observation suggests a further reduction in the Laves phase's volume fraction due to WC addition. The most prominent change is the splitting of the melting peak from a single event into two connected endothermic peaks. In addition, increasing WC content alters the relative intensities of these peaks, with the lower-temperature peak becoming progressively more pronounced compared to the higher-temperature one. The lower-temperature peak is most likely associated with the dissolution of the MC carbides. A systematic shift of this peak toward higher temperature with increasing WC content is evident, indicating both more MC carbides in the microstructure and their enhanced thermal stability. This behaviour is most likely driven by a change in carbide chemistry, from the (Nb, Mo)C-type carbides typical of Alloy 718 to more complex carbides incorporating W. The peak temperatures corresponding to MC carbide dissolution are 1312 °C, 1326 °C, and 1335 °C for WC additions of 2.5, 3.75, and 5 wt%, respectively. He et al. [39] noted that the molten pool, containing WC particles suspended in a Ni-rich liquid, is a reactive environment where multiple metallurgical and chemical processes occur. Upon heating, WC decarburizes, forming W_2C or sub-stoichiometric WC_x phases. In composites of Inconel 718 with WC, the particles can participate in sequential dissolution–diffusion reactions, including $2\,WC \rightarrow W_2C + C$ and subsequent $W_2C \rightarrow 2\,W + C$ [40]. The second endothermic peaks, which are associated with the melting of the γ matrix, are also observed in the DSC curves. The temperatures of these peaks fall within a very narrow interval and show a slight downward trend with increasing WC content, decreasing from approximately 1364 °C to 1354 °C. These values remain very close to those measured for the Alloy 718 (1362 °C). Overall, the modification of Alloy 718 by the addition of WC NPs enhances the thermal stability of the strengthening precipitates while preserving solidus and liquidus temperatures comparable to those of the base material.

The crystallization enthalpy of Alloy 718, determined by integrating the area under the principal exothermic peak (Fig. 3a), equals 146 J/g. This value closely matches the alloy's melting enthalpy, indicating thermodynamic consistency and confirming the reversible character of the observed phase transformations under assumed experimental conditions. The cooling of Alloy 718 shows solidification onset at 1344 °C (liquidus, T_L), determined from the extrapolated beginning of the first exothermic peak, which has a minimum at 1339 °C. A subsequent exothermic peak, with an onset at 1160 °C and a minimum at 1156 °C, is attributed to Laves phase precipitation. Knorovsky et al. [41] reported a γ/Laves eutectic reaction near 1200 °C in Inconel 718, underscoring the influence of niobium segregation on Laves phase formation and its later dissolution during heating. Solidification in all Alloy 718 + WC composites starts through the $L \rightarrow \gamma$ reaction, with T_L varying between 1315 and 1302 °C (Fig. 2b). A shift in the solidification peak of Alloy 718 +WC composites toward lower temperatures and also splitting into two peaks was observed. In the 1.25% WC variant, this second, very fine effect is observed at 1252 °C and is associated with the precipitation of MC carbides. For higher WC addition, the peak associated with the precipitation of MC carbides becomes increasingly pronounced, and its temperature gradually increases to approximately 1296 °C in the Alloy 718 + 5.0% WC variant. The gradual increase in the carbide precipitation rate may indicate a change in the chemical composition. Thermo-Calc simulations also indicated that increasing the W and C concentration in Alloy 718 raises the carbide solvus temperature. Only small thermal effects from Laves phase precipitation are observed in Alloy 718 +WC composites, suggesting a significant reduction in its volume fraction below the detection threshold. Quantitatively, the thermal effect associated with the precipitation of γ/Laves eutectics is negligible in the overall heat balance of the phase changes taking place during solidification. A peak associated with this process is observed in the temperature range of 1072 °C (1.25% WC) – 1129 °C (5% WC). Our results provide compelling confirmation of Cieslak et al. [42] conclusion that increased carbon content promotes MC carbide formation at the expense of Laves-phase precipitation in Nb-bearing Ni-based superalloys. Consistent with this, He et al. [39,40] showed for Inconel 718 reinforced with 40–60 wt% WC fabricated by laser-directed energy deposition that dissolved WC acts as a reservoir of W and C. This reservoir drives NbC formation ($Nb + C \rightarrow NbC$) and can facilitate η-$(Fe_3W_3)C$ formation from reactions involving WC, W, and the liquid. Gibbs-energy trends clearly indicate that W_2C becomes increasingly favoured at elevated temperatures, rendering it easier to form than WC in the molten matrix. However, because W_2C is metastable, solidification shifts the thermodynamic stability toward WC, leading the initially precipitated W_2C to break down and convert to WC.

The ex-situ added WC nanoparticles possess a high surface-to-volume ratio, which significantly accelerates their dissolution in the molten Alloy 718 matrix. Consequently, the dissolution time of nanoparticles is orders of magnitude shorter than that of conventional micron-sized particles. The absence of WC or W_2C carbides in this study can therefore be explained by several thermodynamic and kinetic factors, including the stronger Nb–C bonding and the early nucleation of Nb-rich MC carbides. During the solidification of Alloy 718, Nb exhibits strong microsegregation toward interdendritic regions, which significantly influences carbide precipitation. MC carbides nucleate rapidly in the Nb-enriched liquid because niobium has a stronger chemical affinity for carbon than tungsten. Nb-rich carbides act as effective carbon sinks that suppress the formation of other carbide types. As a result, the available carbon is preferentially consumed by Nb during carbide nucleation, leaving a lack of carbon available for the reprecipitation of WC or W_2C carbides. Furthermore, the MC carbide lattice can dissolve

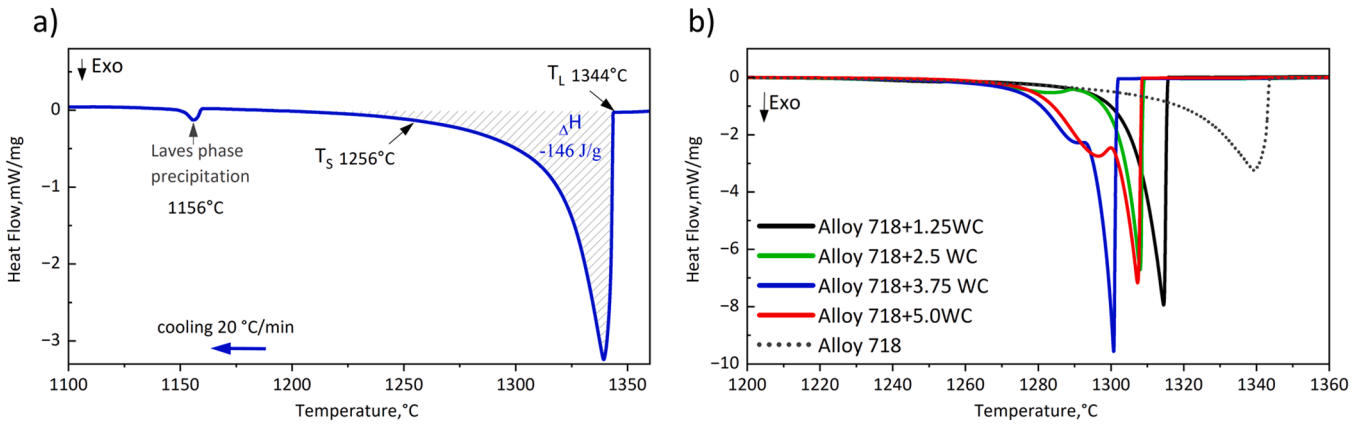

Fig. 3. DSC curves recorded during cooling from liquid state: a) Alloy 718; b) Alloy 718 with WC.

other metallic elements, such as Mo and W, forming more chemically complex carbides. Instead of forming separate WC or W_2C carbides, tungsten atoms are therefore incorporated into the existing Nb-rich MC carbides and play a role in the solid-solution strengthening.

The coefficient of thermal expansion (CTE) is a key parameter in the design of materials for temperature service, particularly for repair applications of Ni-based superalloys. Differences in thermal expansion among various strengthening phases can lead to stress accumulation during heating and cooling cycles, thereby promoting cracking and premature failure. Therefore, understanding the dilatometric behaviour of Alloy 718 modified with WC NPs is essential for evaluating its suitability as a repair material. Fig. 4a presents the dilatometric curves of Alloy 718 and its WC-modified versions recorded during continuous heating. In all cases, the elongation increases with temperature, confirming typical thermal expansion behaviour. A slight increase in the slope of the dilatation curves is observed with increasing temperature, indicating a gradual acceleration of expansion. At the maximum temperature of 1240 °C, the reference Alloy 718 exhibits the highest total elongation, reaching approximately 2.21%. The incorporation of WC nanoparticles results in a systematic reduction in the maximum elongation to 2.18%, 2.04%, 1.93%, and 1.86% with increasing WC NPs content, demonstrating that their addition effectively suppresses the overall thermal expansion of Alloy 718. The calculated CTE values, summarized in Fig. 4b, decrease progressively with increasing WC fraction. This behaviour can be attributed to the intrinsic thermal expansion characteristics of the individual phases. The γ Ni matrix has a relatively high CTE due to its metallic bonding and chemical composition, whereas strengthening phases, such as intermetallics and carbides, exhibit lower CTEs [43]. Tungsten carbide, in particular, has a low CTE, and its presence in the matrix can limits macroscopic elongation [13]. Consequently, increasing the WC NPs content can reduce the effective thermal expansion of the Alloy 718 +WC composites. With increasing temperature, partial dissolution of strengthening precipitates occurs, leading to a gradual increase in the γ matrix volume fraction. This microstructural evolution is reflected in a slightly higher expansion rate at elevated temperatures. From an application perspective, the thermal expansion behaviour of Alloy 718-based materials is particularly relevant for repair technologies such as welding, brazing, or additive manufacturing, where compatibility between the repair material and the substrate is critical. In advanced power-generation systems and aerospace components, Ni-based superalloys are often joined to materials with lower thermal expansion coefficients, such as cobalt-based alloys. Mismatch in CTE at dissimilar joints can induce significant internal stresses during thermal cycling, accelerating fatigue crack initiation and damage accumulation over the long term. The reduced thermal expansion observed in Alloy 718 +WC composites may therefore help mitigate CTE mismatch and enhance the durability of repaired components under cyclic thermal loading.

3.2. *Influence of the WC NPs addition on the as-cast microstructure and phase composition of Alloy 718*

The synchrotron X-ray diffraction patterns of Alloy 718 and Alloy 718 +WC composites are shown in Fig. 5a. All diffractograms are dominated by intense reflections indexed to the (111), (200), and (220) planes of the FCC Ni-rich γ-matrix. In the reference Alloy 718, peaks associated with the Laves phase and MC carbides are clearly visible. Although the incorporation of WC does not introduce new phases, systematic changes in peak intensities and slight shifts in peak positions are evident, suggesting alterations in lattice parameters and phase

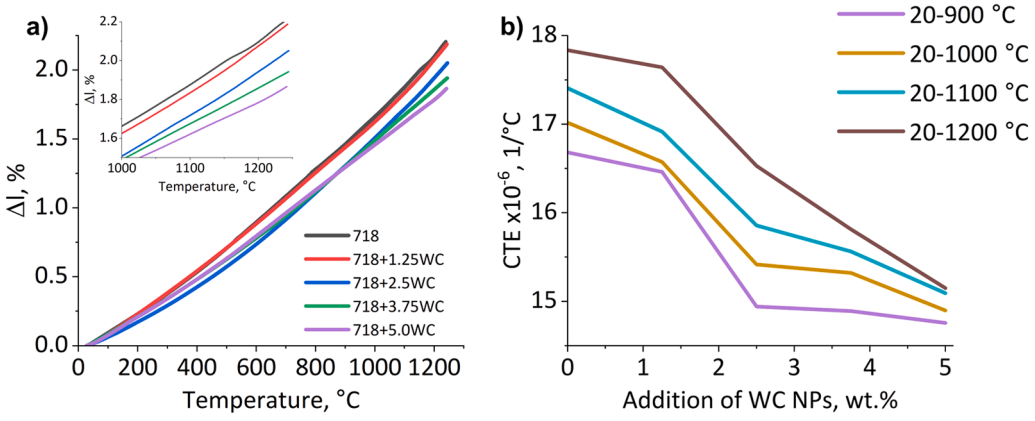

Fig. 4. Dilatometry of Alloy 718 +WC composites: a) Δl; b) CTE.

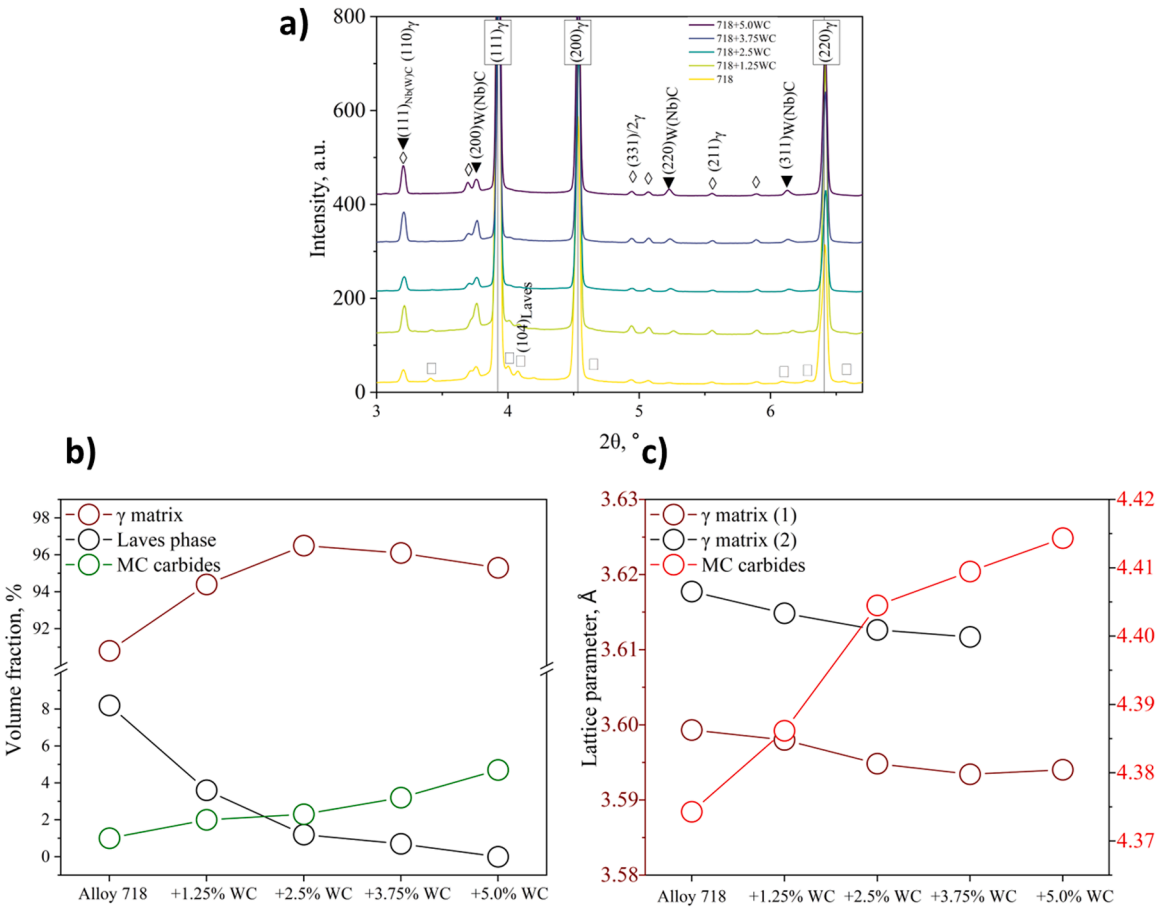

Fig. 5. a) X-ray synchrotron diffraction pattern of the ex-situ Alloy 718 +WC nanocomposites processed via suction casting; b) influence of WC addition on volume fraction of γ matrix, Laves phase and MC carbides; c) influence of WC addition on the lattice parameter of γ matrix and MC carbides.

distributions. These effects were examined through Rietveld refinement to enable a quantitative comparison between the investigated variants. Change of the WC NPS addition also influences the relative proportions of the constituent phases (Fig. 5b). In the reference Alloy 718, the γ matrix accounts for 90.8%, with the remaining fraction comprised of the Laves phase (8.2%) and MC carbides (1.0%). Introducing WC NPs into Alloy 718 leads to a progressive reduction in the Laves phase fraction. The measured values decrease from 3.6% at 1.25% WC to 1.2% at 2.5% WC and 0.7% at 3.75% WC, while the Laves phase is no longer detected in the variant containing 5.0% WC, demonstrating a systematic decline. This reduction is advantageous because it mitigates the detrimental influence of the Laves phase on material performance during subsequent heat treatment and service. Concurrently, the volume fraction of MC carbides increases steadily with WC addition, from approximately 2% for Alloy 718 + 1.25% WC to about 4.7% for Alloy 718 + 5.0% WC. Changes in phase volume fractions caused by adding WC NPs to Alloy 718 are accompanied by alterations in lattice parameters, which are summarized in Fig. 5c. For the γ phase, two distinct lattice-parameter regions are observed in the base alloy and in samples containing up to 3.75% WC, indicating solute element segregation during suction casting and resulting compositional differences between dendritic and interdendritic γ regions. As WC content increases, the matrix lattice parameter decreases slightly, demonstrating that higher NPs content reduces microstructural heterogeneity and encourages a more uniform alloy structure. At 5.0% WC, the γ phase exhibits a single lattice parameter, confirming the reduction of heterogeneity. Increasing the WC NPs content affects not only the lattice parameter of the γ matrix but also that of the MC carbides. A pronounced variation in the MC lattice parameter is detected, indicating partial dissolution of WC, involving both incorporation of W and C into the matrix and substitution of Nb by W within the carbide lattice. From the Ni–W and Ni–C binary phase diagrams, the maximum solubilities are approximately 17.5 at% W and 2.7 at% C, respectively. The surplus solute segregates to form MC carbides. Owing to the strong carbide-forming tendency of Nb and its partial replacement by W, a systematic increase in the MC lattice parameter is recorded, rising from 4.3861 Å at 1.25% WC to 4.4143 Å at 5.0% WC. This trend is consistent with W's larger atomic radius relative to Nb. It indicates that the W content in the MC carbides increases progressively with increasing initial WC NPs addition to the feedstock.

Microstructural examination confirms that both the reference Alloy 718 and the WC-modified variants solidify with a typical dendritic morphology (Figs. 6–8). During solidification, non-uniform solute redistribution occurs between dendrite cores and interdendritic regions, leading to microsegregation and promoting the formation of secondary precipitates within the interdendritic liquid. This behaviour is consistent with the well-established mechanism in which solute elements are rejected into the residual melt and subsequently undergo partial back-diffusion, leading to continuous solute exchange between the solid and liquid phases [44]. To quantitatively assess this segregation behaviour, partitioning coefficients were calculated based on SEM–EDX measurements as the ratio of the average alloying element concentration in dendrite cores to that in interdendritic regions. The results clearly demonstrate that the addition of WC NPs influences the partitioning behaviour of all investigated alloying elements (Table 3). Nickel, the principal constituent of the γ matrix, exhibits partitioning coefficients slightly above unity (k^{Ni}=1.037–1.066), indicating mild enrichment in dendrite cores. Owing to the high concentration of strong carbide-forming elements in the alloy system, Fe primarily contributes

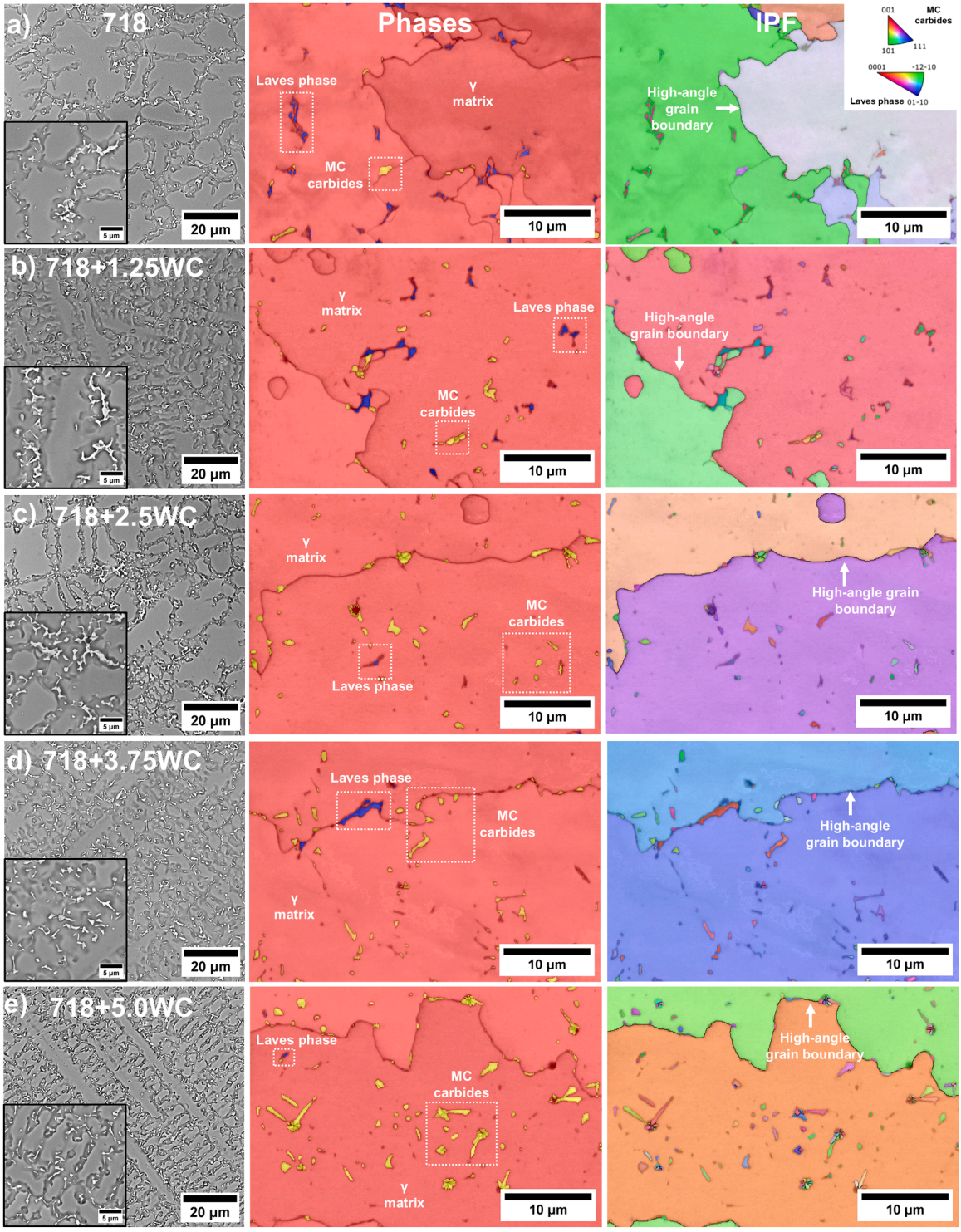

Fig. 6. As-cast microstructure of produced Alloy 718 +WC nanocomposites with corresponding SEM-BSE images and EBSD (IPF: Inverse Pole Figure): a) 0%; b) 1.25%; c) 2.5%; d) 3.75%; e) 5.0%.

to solid-solution strengthening of the γ phase, which explains the consistently observed $k^{Fe} > 1.0$. The enrichment of Ni and Fe in dendrites supports the preferential formation of precipitates in interdendritic regions, as increasing fractions of Ni- and Fe-depleted precipitates locally reduce their concentrations in the interdendritic liquid. Chromium, which contributes both to solid-solution strengthening and to the formation of secondary phases, shows partitioning coefficients close to unity (k^{Cr}=0.994–1.003) in the WC-modified variants. Although Cr is known to participate in carbide formation, its segregation tendency is moderated by the presence of stronger carbide-forming elements. In contrast, Nb and Mo exhibit partitioning coefficients significantly below unity in all investigated variants, indicating strong segregation toward interdendritic regions. In particular, Nb shows pronounced segregation, consistent with its key role in the formation of primary strengthening precipitates. A systematic decrease in k^{Nb} with increasing WC content suggests compositional changes in interdendritic precipitates, likely related to partial dissolution of WC NPs during melting, which enables Nb to participate in the formation of more MC carbides, as confirmed by

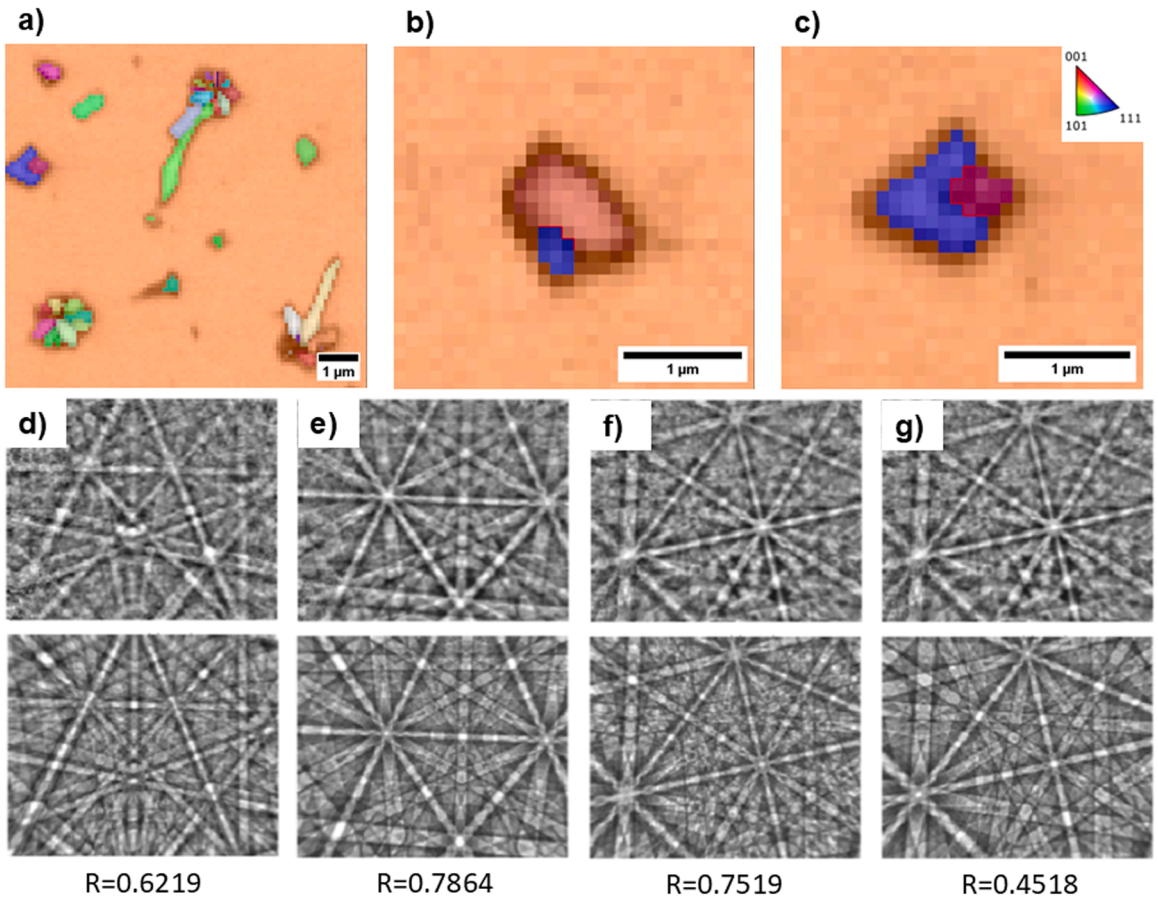

Fig. 7. a-c) EBSD IPF maps of MC carbides; Comparison of experimental (top) and dynamically simulated (bottom) diffraction patterns with corresponding normalized cross-correlation coefficients R: d) Laves phase (C14); e) Ni matrix; f) MC carbide fitted with NbC simulation; g) experimental MC pattern fitted using a Ni simulation.

synchrotron XRD analysis. W exhibits $k > 1$, which can be attributed to its low diffusivity and the high cooling rates characteristic of suction casting, limiting its redistribution during solidification.

Fig. 7a shows an IPF map of MC carbides crystallized in a flower-like morphology, which may suggest heterogeneous nucleation on a solid particle. Figs. 7b and 7c present examples of individual MC carbide particles containing Σ3 twin boundaries, highlighted in red. Such twinned NbC carbides are frequently observed in rapidly solidified Ni-based alloys [45]. Fig. 7d shows an experimental diffraction pattern of the Laves phase fitted using a dynamical simulation of Fe_2W with a hexagonal C14 ($MgZn_2$-type) structure. Figs. 7e and 7 f present dynamical simulations of Ni and MC, respectively, fitted to the experimental diffraction patterns of the matrix and NbC carbides. Since conventional Hough transform–based EBSD indexing relies mainly on interplanar angles, it cannot reliably distinguish MC carbides from the Ni matrix due to their identical angular relationships. In contrast, dynamical template matching enables unambiguous phase discrimination. This is demonstrated in Fig. 7 g, where fitting a simulated Ni pattern to an experimental NbC pattern yields a significantly lower correlation coefficient (R=0.4518) than the correct MC–NbC match, with a difference of 0.3001. This confirms the robustness of the dynamical approach for reliable phase identification.

Based on the microstructural examination, it can be observed that Nb-rich Laves phase precipitates and blocky MC carbides are the main strengthening precipitates in as-cast Alloy 718. MC carbides constitute a stable and essential component of Ni-based superalloys, owing to their high thermodynamic stability at elevated temperatures. However, the volume fraction of MC carbide precipitates in the reference Alloy 718 is limited by the low carbon content. The Laves phase, characterized by a hexagonal hP12 structure (space group P6/mmc), is an A_2B-type intermetallic in which Ni, Fe, and Cr occupy the A sites and Nb, W, and Mo occupy the B sites [46]. The Laves phase is generally regarded as detrimental because it locally depletes the γ matrix of Nb and adversely affects mechanical properties. The Laves phases, arranged in long, continuous chains, can facilitate both the onset and propagation of cracks, thereby increasing crack susceptibility and degrading material toughness. Such cracking behaviour also favours the detachment of large wear particles, resulting in three-body abrasive wear [47]. However, because Laves phase precipitation is difficult to mitigate in Nb-bearing alloys, understanding the factors controlling its morphology, distribution, and volume fraction is particularly important. The Laves phase typically occurs either as isolated particles or as elongated, chain-like precipitates. Under rapid cooling, such as during suction casting, the development of morphologically complex Laves phase is significantly suppressed due to the limited time available for diffusion-controlled growth, as evidenced by SEM-BSE and SEM-EBSD images. Increased cooling rates lead to enhanced undercooling of the liquid, thereby increasing the excess free energy and favouring rapid nucleation over extensive growth of liquid–solid interfaces. Kumara et al. [48] demonstrated that the formation of the Laves phase cannot be fully suppressed even under strongly non-equilibrium solidification conditions encountered during AM, despite melt pool cooling rates approaching 10^5 °C s^{-1} . Mohammadpour et al. [49], in their investigation of single-track laser powder bed fusion of Nb-containing Inconel 625, also showed that both the morphology and Nb content of Laves phase precipitates are highly sensitive to solidification conditions, particularly cooling rate and solidification time. An increased cooling rate limits Nb segregation by reducing the time available for solute

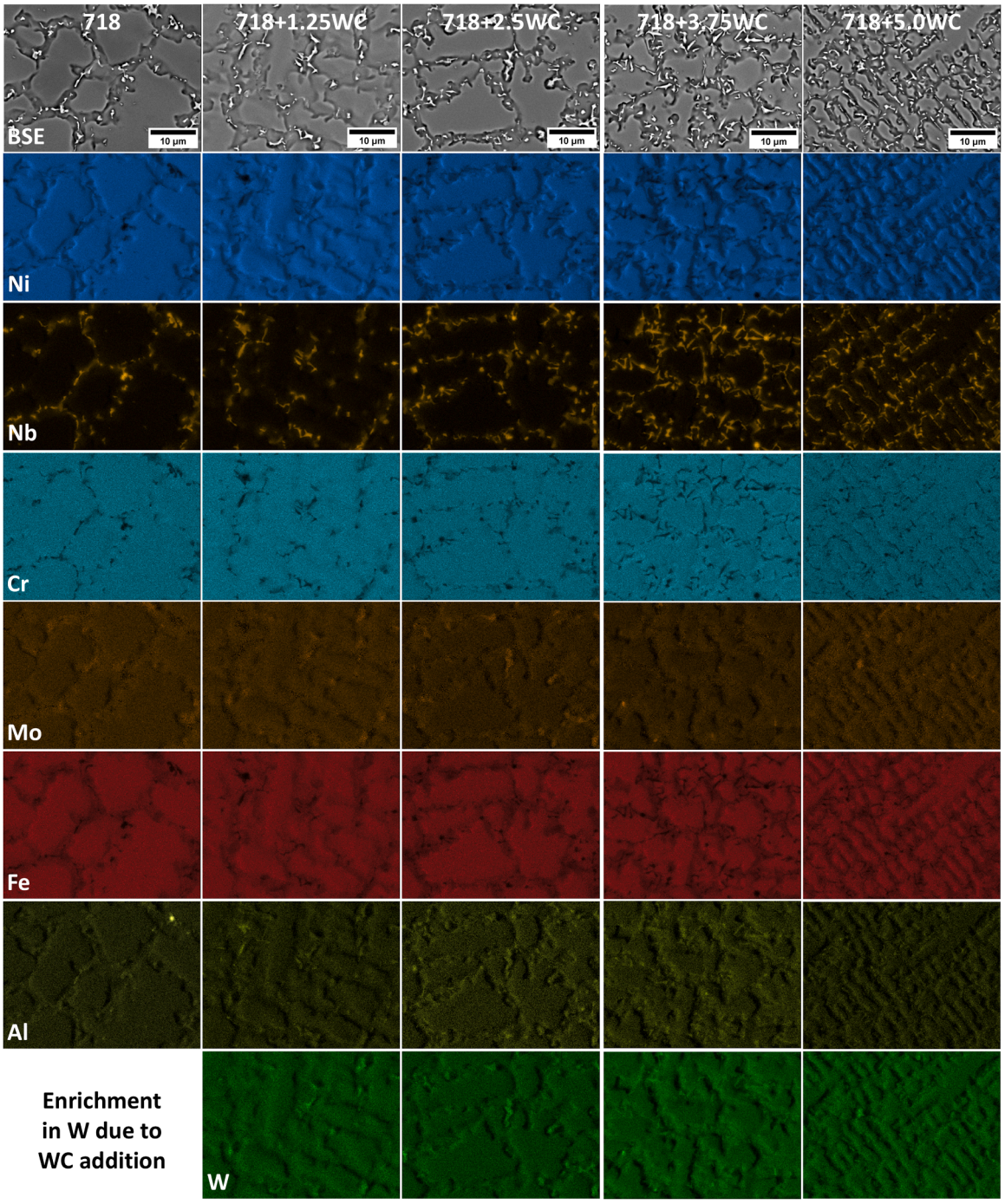

Fig. 8. SEM-EDX mapping of selected alloying elements in the Alloy 718 +WC composites.

Table 3
Influence of the WC NPs addition on the partitioning coefficients of alloying elements in Alloy 718.

Element Variant	Ni	Cr	Fe	Nb	Mo	W
718	1.039 (0.003)	0.994 (±0.003)	1.092 (±0.007)	0.262 (±0.007)	0.854 (±0.032)	-
718 + 1.25WC	1.037 (±0.005)	1.003 (±0.003)	1.091 (±0.007)	0.259 (±0.026)	0.869 (±0.053)	1.120 (±0.034)
718 + 2.5WC	1.045 (±0.007)	0.991 (±0.004)	1.085 (±0.021)	0.251 (±0.08)	0.878 (±0.104)	1.152 (±0.075)
718 + 3.75WC	1.052 (±0.003)	0.998 (±0.031)	1.078 (±0.003)	0.246 (±0.005)	0.884 (±0.032)	1.093 (±0.010)
718 + 5.0WC	1.066 (±0.009)	0.984 (±0.003)	1.088 (±0.018)	0.199 (±0.020)	0.827 (±0.056)	1.039 (±0.012)

redistribution, while higher solidification rates promote solute trapping within the γ matrix. This mechanism suppresses excessive Nb enrichment in the residual liquid, thereby reducing the driving force for Laves phase formation. Consequently, rapid solidification processes

such as suction casting retain a larger fraction of Nb within the γ matrix, lowering both the Nb concentration in the remaining liquid and the volume fraction of the γ+Laves eutectic. These findings indicate that complete elimination of the Laves phase during casting and deposition processes is impractical. Therefore, microstructural control via chemical composition modification or heat treatment should focus on minimizing its size and volume fraction. Studies on Alloy 718 exposed to 1150 °C, slightly below the melting onset, have shown that the Laves phase gradually dissolves as the holding time increases. Consequently, Nb-enriched regions diminish, and the volume fraction of the Laves phase decreases. It is attributed to back-diffusion of solute atoms from enriched zones into the surrounding γ phase, driving the alloy toward a more uniform composition. This homogenization is driven by the system's tendency to remove metastable, non-equilibrium phases. Mathematical predictions of the dissolution kinetics suggest that complete dissolution of the Laves phase in 1150 °C can occur after 28 h [38].

Although the overall morphology of the precipitates in interdendritic spaces of Alloy 718 +WC composites does not change significantly, consistent with the identical phase composition identified by synchrotron radiation study, a noticeable refinement of interdendritic precipitates is observed in variants containing 3.75% and 5.0% WC. Refinement of precipitates can reduces this stress concentration effect because smaller particles distribute stresses more uniformly within the surrounding matrix. As a result, the probability of crack initiation at carbide interfaces decreases. Under the electric arc, WC NPs become thermodynamically unstable and readily dissolve into the molten Alloy 718 due to their relatively low enthalpy of formation ($\Delta H°_{f,WC} = -42.3 \pm 0.8$ kJ/mol for $T < 1575$ K) [50]. The reduction in the Laves phase volume fraction, accompanied by an increase in MC carbides, may be attributed to several factors. First, the precipitation temperature of the Laves phase decreases with the addition of WC, leaving insufficient time for its formation. Second, during the early stages of solidification, Nb and Ti in the melt are consumed through reactions with carbon to form (Nb, Mo, Ti, W)C carbides. As a result, the interdendritic liquid becomes depleted in Nb, making Laves phase precipitation more difficult. The amount of reinforcement also controls the degree of constitutional supercooling ahead of the solid–liquid interface, which can induce solute redistribution and promote in-situ nucleation. Dissolution of the ex situ WC NPs releases carbon, leading to its gradual segregation along grain boundaries, lowering grain-boundary energy and enhancing nucleation, as also stated by Pan et al. [51]. Furthermore, MC carbides decorating the grain boundaries, as observed in SEM–EBSD images, reduce the driving force for grain growth and impose a drag effect, thereby decreasing boundary mobility and suppressing growth along the direction of the maximum thermal gradient. This mutual change in the volume fractions of the Laves phase and MC carbides can be considered a positive development for further service. Stepanova et al. [52] showed that finely dispersed, blocky MC carbides improve yield and ultimate tensile strength in Ni-based superalloys compared with script-like morphologies. Cai et al. [53] reported that coarse, skeleton-like MC carbides promote instability and cracking, leading to a pronounced reduction in ductility.

Analysis by TEM-SAED and FFT of precipitation-free zones confirms the presence of an FCC γ matrix, without detectable diffraction patterns corresponding to intermetallic γ′ (Ni_3Al) or γ″ (Ni_3Nb) phases (Fig. 9). This absence indicates that the high cooling rates during solidification suppress the formation of these precipitates, while these phases can appear after heat-treatment. The mechanical performance of unmodified Alloy 718 (Inconel 718) is primarily governed by a γ-phase matrix strengthened by γ′ and metastable γ″ precipitates [35]. The SAED pattern of precipitates confirmed that the MC carbides exhibit an FCC crystal structure, belonging to the Fm-3m (225) space group, with a lattice

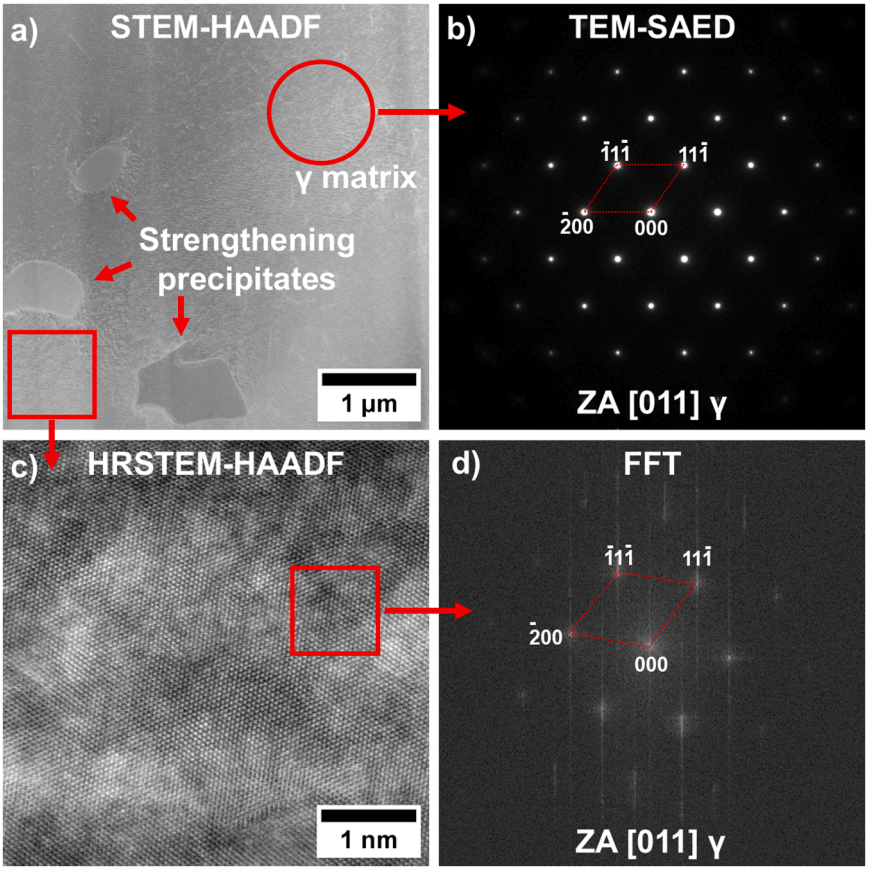

Fig. 9. γ phase: a) STEM-HAADF image; b) SAED pattern; c) nanostructure of γ phase; d) FFT.

parameter of 4.374–4.414 Å depending on the initial WC NPs addition (Fig. 10). These carbides have relatively smooth and well-defined edges, indicating a stable growth morphology during solidification. The enrichment in Nb and Mo (to a lesser extent, Ti and W) of these carbides suggests that these elements segregate strongly during solidification, which promotes the preferential formation of stable MC carbides. Zhang et al. [54] reported in Ni-rich alloy composites containing 45 wt% WC fabricated by plasma arc welding, where coarse WC carbides (>100 μm) were found to be unstable under the high thermal energy density of the process, leading to partial dissolution and localised reprecipitation. A reaction layer with needle- and strip-like morphologies developed around retained WC particles, while blocky carbides enriched in W, Cr, and C formed at the periphery of the reaction zone. These carbides were attributed to WC_x and M_xC_y-type phases, including M_6C and Cr-rich carbides. In our study, we did not observe such precipitates at the interfaces on TEM-BF images, so the mechanism of new precipitate formation can differ. Thermodynamic calculations, together with microstructural observations, show that MC carbides are the predominant secondary phase, particularly at higher WC additions. Consequently, these carbides play a major role in governing the alloy's solidification behaviour. During solidification of Alloy 718 containing WC-NPs, the solute content ahead of the solid–liquid interface is altered by the introduced elements in the γ matrix. When the liquidus temperature exceeds the actual solidification temperature, an extended constitutional supercooling zone (CSZ) forms, promoting nucleation. Tan et al. [55] reported that the growth-restriction factor can quantify the evolution of the constitutional supercooling zone, Q (Eq.4):

$$Q = m(k-1)C_0 \tag{4}$$

Where: m - liquid curve slope; k - coefficient of solute distribution; C_0 - solute concentration.

Based on the W–Ni binary phase diagram, the Q for tungsten in the nickel alloy is 0.3 K [56], pointing out that constitutional supercooling is limited due to the relatively low Q value of WC, so grain refinement is driven by in-situ Nb-rich carbides formation. The interfacial energy associated with heterogeneous nucleation can be estimated using Eq. 5. [57]:

$$\Delta G_{het} = \left[\left(\frac{4\pi}{3}\right) r^3 \Delta F_V + 4\pi r^2 \gamma\right] \bullet \left[\frac{2 - 3\cos\theta + \cos^3\theta}{4}\right] \tag{5}$$

where r-radius; ΔFV- free energy of per volume; γ- interfacial energy; θ- wetting angle

A high wetting angle and elevated interfacial energy can impede nucleation. However, TEM–BF images show that MC carbides exhibit crystallographic relationships with the matrix, and the precipitates are fine, especially those exhibiting spherical shapes. Such features render these carbides ideal nucleation sites during the solidification of Alloy 718, thereby increasing the nucleation density.

3.3. *Influence of the WC NPs on the steam oxidation and Ar+ 0.25%SO_2 gas mixture resistance of Alloy 718*

Fig. 11a presents the steam oxidation behaviour of Alloy 718 with WC additions over 1000 h, demonstrating that WC significantly affects the oxidation performance. The WC-free reference variant shows accelerated early oxidation, reaching 0.184 mg/cm^2 at 1000 h. Introducing 1.25% WC reduced this value nearly in half to 0.097 mg/cm^2, and higher WC levels further reduced mass gain to ~0.059 mg/cm^2, for 3.75 and 5.0% WC, small mass decreases appear beyond ~500 h. It cannot be ruled out that this is due to the local volatilization of WO_3. This volatilization effect is minor overall, as all WC-modified specimens still exhibit net mass gain with time. No spallation occurred during the exposure, confirming that the oxide scale remained firmly bonded to the Alloy 718-based substrate. The early, steep mass increase corresponds to a transient, accelerated oxidation regime, followed by a transition to steady-state behaviour as a compact protective oxide scale forms [58]. Progressing oxidation slows down because scale thickening lengthens diffusion paths, and the reactions become diffusion-controlled when the

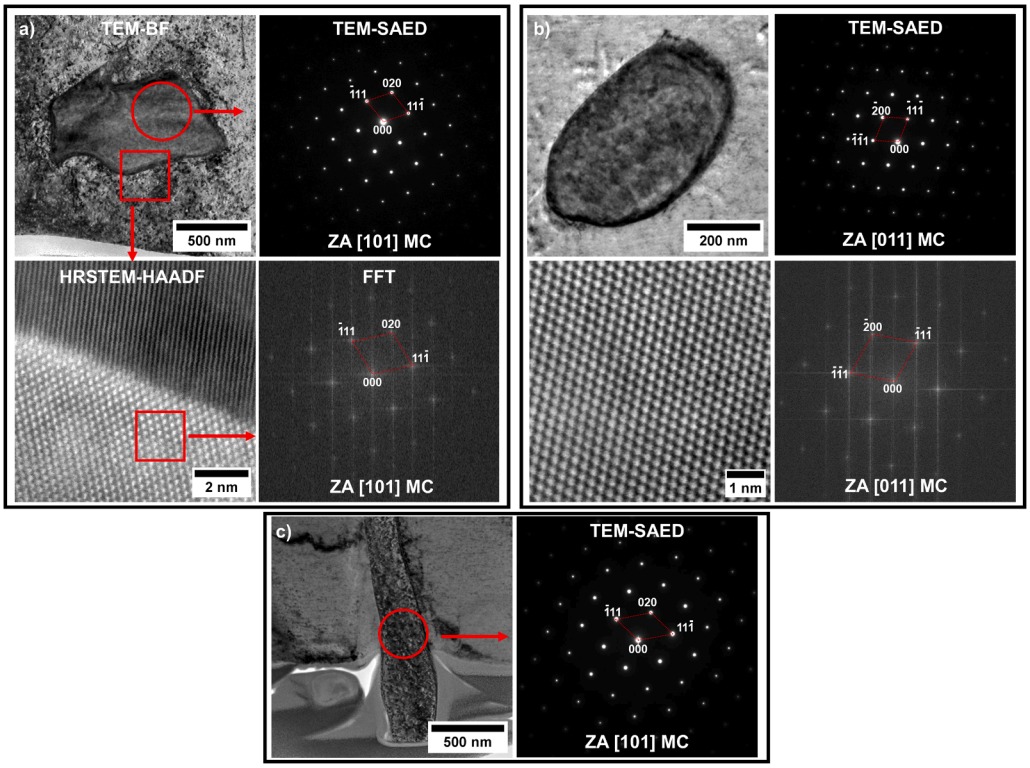

Fig. 10. Microstructure and nanostructure of the MC carbide in the interdendritic space, with corresponding TEM-SAED pattern and FFT analysis: a) blocky-shaped carbide; b) spherical-like carbide; c) plate-like carbide.

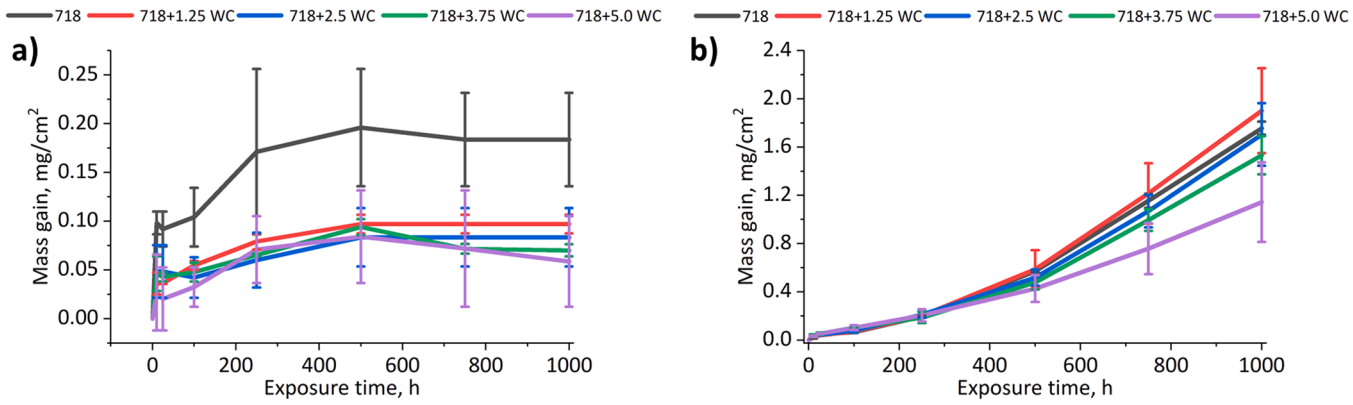

Fig. 11. Mass gain of Alloy 718 and 718 +WC composites registered during experiment in: a) steam, b) Ar+ 0.25%SO_2 gas mixture at 704 °C.

parabolic rate constant of the oxide scale growth prevails. It was found that the greater the WC addition to Alloy 718, the greater the mass reduction. However, the highest addition of WC to Alloy 718 is slightly less beneficial than the addition of 1.25 or 2.5%, because the addition of 1.25 and 2.5% showed steady state mass gain of exposed material in contrast to the specimen with 5.0%, where mass gain between 500 – 1000 h of exposure was strongly reduced. This reduction could be due to volatilization of WO_3 [59].

Exposure of WC-modified Alloy 718 to Ar + 0.25% SO_2 led to pronounced changes in its high-temperature behaviour. The kinetics differ markedly from those observed in steam (Fig. 11b). The specimens subjected to SO_2-containing gas exhibited substantially higher mass gains than those exposed to an oxygen-rich environment, and the distinctly different curve shapes indicate a fundamentally different scale-formation mechanism under gas-mixture conditions. The reference Alloy 718 showed an average mass gain of 1.757 mg/cm^2. Introducing 1.25% WC slightly increased mass gain to 1.902 mg/cm^2, however, further WC additions led to progressive reduction, demonstrating greater resistance in the aggressive SO_2-containing atmosphere, with 2.5% WC, mass gain decreased to 1.705 mg/cm^2, below that of the unmodified alloy and at 5.0% WC it fell to 1.144 mg/cm^2, representing nearly a 35% mass gain reduction. These results clearly demonstrate that WC additions improve the corrosion resistance of Alloy 718 in SO_2-containing gas mixture. The contrasting mass gain profiles between Ar+ 0.25% SO_2 and steam exposures further underscore that different oxide-scale compositions and growth mechanisms operate in these atmospheres, emphasising the dominant influence of environment on protective-scale development at high temperature. The reaction-rate exponents (n) are below the ideal parabolic value of 0.5 for all steam-exposed variants, indicating sub-parabolic kinetics. Rather than exhibiting parabolic growth, the behaviour is better described by a cubic rate law, in which the mass gain of the exposed specimen is controlled by short-circuit diffusion [60]. This short-circuit diffusion occurs along high-diffusivity paths, such as grain boundaries or dislocations. It is particularly significant at low temperatures, small grain sizes, and high defect densities. Based on this, the temperature of 704 °C was slightly too low to achieve an n value greater than 0.3, indicating pure volume diffusion, as observed in a diffusion-controlled process with n = 0.5 (Table 4). Furthermore, the value of n = 0.1 for the specimens with additions of 2.5, 3.75, and 5% indicates that the oxide scale developed on those specimens indicates extremely slow, restricted protective kinetics (often logarithmic). This value (n = 0.1) indicates that oxide scale growth is much slower than under cubic or near-cubic behaviour. Such behaviour is observed in the reference specimen and in the 1.25% WC samples. Thus, the exposure temperature when adding WC was too low to develop an oxide scale controlled by a pure diffusional process, which would reach n = 0.5. Short-circuit diffusion implies the formation of microvoids within the oxide scale. These microvoids nucleate at stress concentrators, such as grain boundaries, triple points, or inclusions [61]. Short-circuit diffusion acts as a high-speed path. It allows atoms to move away from the void tip or vacancies into the void, causing it to grow [62,63]. The Alloy 718 +WC nanocomposites tested in a gas mixture containing SO_2 showed n values approaching 1.0. This indicates almost linear oxidation kinetics, which are controlled primarily by surface chemical reactions rather than diffusion processes, as observed for the steam-exposed samples [64]. These results are consistent with well-known oxidation models. Such models predict that S-rich environments produce less protective oxide scales that are porous and thicken rapidly, leading to higher overall mass gain [65,66].

Table 4
Calculated time exponents (*n*) for Alloy 718 and WC-NPs-modified variants.

Addition of WC into Alloy 718, wt%	n for steam	n for Ar+ 0.25% SO_2 gas mixture
0	0.2	1.0
1.25	0.3	0.9
2.5	0.1	0.9
3.75	0.1	0.8
5.0	0.1	0.8

According to the XRD patterns in Fig. 12, Cr_2O_3 was the dominant oxidation product after exposure to steam. This finding aligns with expectations, as the Gibbs free energy of formation for Cr_2O_3 is much lower than that of Ni-rich oxides. The introduction of WC-NPs into Alloy 718 did not affect phase formation after steam oxidation. However, it did influence the mass gain of the exposed specimens. The addition of WC should not have much impact on Cr_2O_3 formation, since Cr_2O_3 was the main phase formed in all cases. The presence of γ-phase peaks in XRD confirms a very thin, protective Cr_2O_3 layer on every exposed specimen in steam. In contrast, after exposure to an Ar+ 0.25% SO_2 gas mixture, the surfaces of both Alloy 718 and Alloy 718 +WC consisted of Cr_2O_3, Ni_3S_2, and Fe_3O_4, regardless of the initial WC addition. The growth of the oxide scale was strongly influenced by reduced partial pressures of oxygen (pO_2) and sulfur dioxide (pSO_2). Thermal exposure promotes SO_2 decomposition. Variations in the $(pO_2)_{(gas)}/(pSO_2)_{(gas)}$ ratio can be inferred indirectly from X-ray diffraction patterns. The presence of Cr_2O_3 confirms that the oxygen partial pressure was sufficiently high for its stabilization. The oxide remains stable whenever pO_2 exceeds its equilibrium pressure $(pO_2)_{(eq)}$. Due to the high Cr content in Alloy 718 and the low Gibbs free energy of Cr_2O_3 formation, this oxide formed first. This was followed by Fe_3O_4 and then Ni_3S_2, as the activity of O_2 is reduced after the formation of Cr- and Fe-based oxides. NiO formation was not observed under either of the tested conditions. According to the Ellingham diagram [65], a more negative ΔG indicates a stronger tendency for phase oxide formation and greater stability (oxide/sulphide) under specific temperature and pressure conditions. Under experimental conditions, Cr_2O_3 exhibits a more negative ΔG than NiO, making its

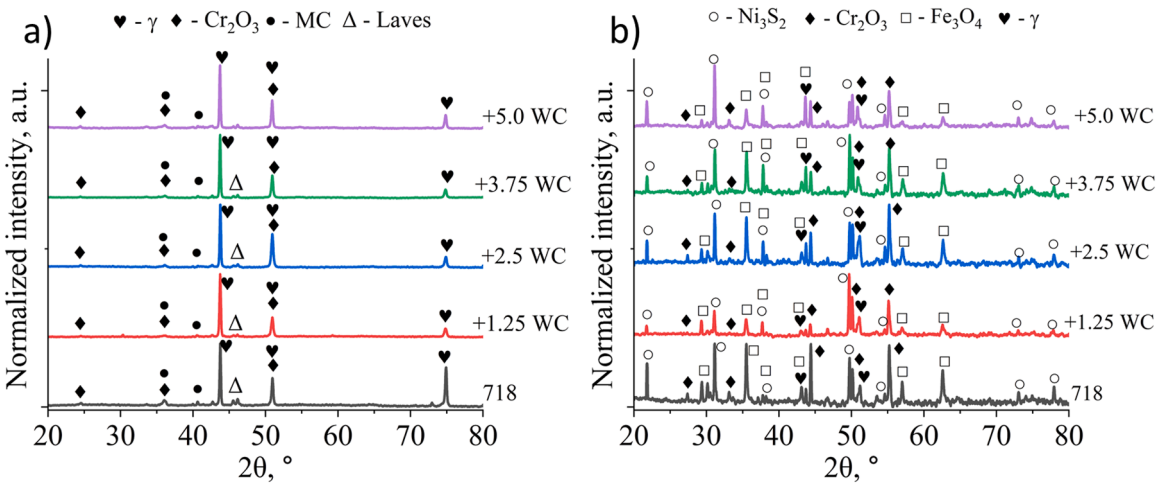

Fig. 12. XRD patterns of oxide-scales formed after oxidation in: a) steam; b) Ar+ 0.25% SO_2 atmosphere.

formation thermodynamically favourable. With approximate concentrations of 20 wt% Cr and 70 wt% Ni, Cr initially promotes the development of a protective oxide scale in oxygen-rich environments. However, the growth of Cr_2O_3 is limited. If Cr activity decreases below a critical threshold due to oxide scale formation, the high Ni activity may lead to the formation of less protective NiO. This work showed no NiO formation. It can be inferred that the Cr_2O_3 oxide scale was protective, and that insufficient oxygen penetrated the scale to allow NiO formation. In general, the NiO phase is detrimental because its cationic defects accelerate oxygen diffusion, increasing mass gain [67], and also serve as a precursor for $NiCr_2O_4$ spinel formation. In this study, neither NiO nor $NiCr_2O_4$ was observed, suggesting, as mentioned earlier, that the Cr_2O_3 layer effectively established a protective barrier, suppressing the formation of non-protective oxides.The presence of SO_2 in the gas phase suggests the potential formation of sulfur-rich phases, however, the relatively low pSO_2 limited this process mainly to Ni_3S_2. Because the sulfur dioxide partial pressure was above the equilibrium pressure ($(pSO_2)_{(eq)}$), Ni_3S_2 could form and remain stable. Compared with oxides, sulfides possess higher Gibbs free energy and contain more crystal defects, which enhance sulfur and nickel diffusion and contribute to the larger mass gains observed in SO_2-containing environments. In hot-end components such as Ni-based superalloy turbine blades, sulfur-containing gases pose a significant corrosion risk [68]. Sulfur reacts with nickel to generate sulfides like Ni_3S_2 and NiS, as well as sulfates, which can accumulate on blade surfaces, alter the microstructure, and reduce overall performance. Moreover, the corrosion products that form during service are prone to spallation, exacerbating material degradation. Fig. 13 shows the surface and cross-sectional microstructures of Alloy 718 modified with WC-NPs, tested in both steam and Ar + 0.25% SO_2 atmospheres. In steam, the oxide scale on Alloy 718 + WC displays a characteristic morphology with flat and rippled oxidation zones. The high oxidation resistance in this environment is attributed to the formation of a strongly adherent Cr_2O_3 layer. Minor localized microvoids are also observed, likely associated with the formation of volatile WO_3. In contrast, exposure to the SO_2-containing atmosphere resulted in significant changes in surface morphology and corrosion products. Surfaces featured numerous precipitates, ranging from simple geometric shapes to more complex forms, markedly different from steam-exposed samples. Reference Alloy 718 formed a brittle oxide scale with poor adhesion, whereas increasing WC content slightly improved adhesion, likely due to a reduction in large blocky precipitates. Rapid formation of a thin Cr_2O_3 layer appears critical for protecting against degradation. Unlike the uniform Cr_2O_3 seen in steam, specimens tested in Ar + 0.25% SO_2 developed poorly adherent Fe_3O_4 and Ni_3S_2. SEM images indicate that Fe_3O_4 often forms within Ni_3S_2 and partially covers it, resulting in a core-like morphology. Although the surface products are similar across Alloy 718 + WC composites, the amounts of Fe_3O_4 and Ni_3S_2 decrease with higher WC content. Furthermore, beneath the surface, a layer of finely mixed M_xO_y and M_xS_y phases was observed, where M includes Ni, Cr, W, Nb, Mo, and Fe. The incorporation of WC into Alloy 718 provides several beneficial effects. Specifically, adding 5% WC reduced mass gain without altering the fundamental mechanism of the oxide scale formation. This decrease in mass gain might be attributed to the interaction of SO_2 with MC carbides. Supporting this, Liu et al. [69] have suggested that metal carbides can effectively trap and neutralize SO_2, promoting its dissociation. As a result, WC could enhance this effect, with Alloy 718 containing the largest WC fraction exhibiting the lowest mass gain. Nevertheless, all exposed specimens exhibited linear-scale growth behaviour, indicating that the influence of WC particles in an SO_2-rich atmosphere is limited. Thus, degradation follows a near-linear pattern, dominated by chemical reactions rather than diffusion-controlled processes.

3.4. Influence of the WC NPs on the hardness and wear resisistance of Alloy 718-based composites

Hardness is one of the key parameters governing the wear behaviour of metal matrix composites, accordingly, hardness measurements were conducted before evaluating dry-sliding wear performance. The unreinforced Alloy 718 shows a hardness of approximately 198 HV10. Progressive incorporation of WC NPs enhances hardness, reaching 198 HV10 at 1.25% WC and rising further to 221 HV10 at 5.0% WC (Table 5).

Wear resistance can be quantified in various ways, including, quite often, by measuring mass loss or the wear rate. The difference between the initial and post-test mass provides a direct way to compare the behaviour of different materials under frictional loading. The general trend is that harder materials exhibit lower wear rates, but excessively hard metal matrix composites (MMCs) can exhibit brittleness, leading to crack initiation and particle extraction from the matrix during friction. Consequently, the best tribological properties are achieved not solely by maximising hardness but by optimising it, for example, by homogeneously distributing the reinforcing phase. Based on dry-sliding test results, the mass loss and corresponding wear coefficient were determined for Alloy 718 and its WC-modified variants. In the reference variant, the mass loss was 0.090%, corresponding to a wear coefficient of 4.56×10^{-8} mg/Nm. Both the mass loss and the wear coefficient after the 1.25% WC addition are very close to the reference values, indicating that the carbide-strengthening phase contributes little to wear at the contact zone. With further increases in WC content in Alloy 718, a

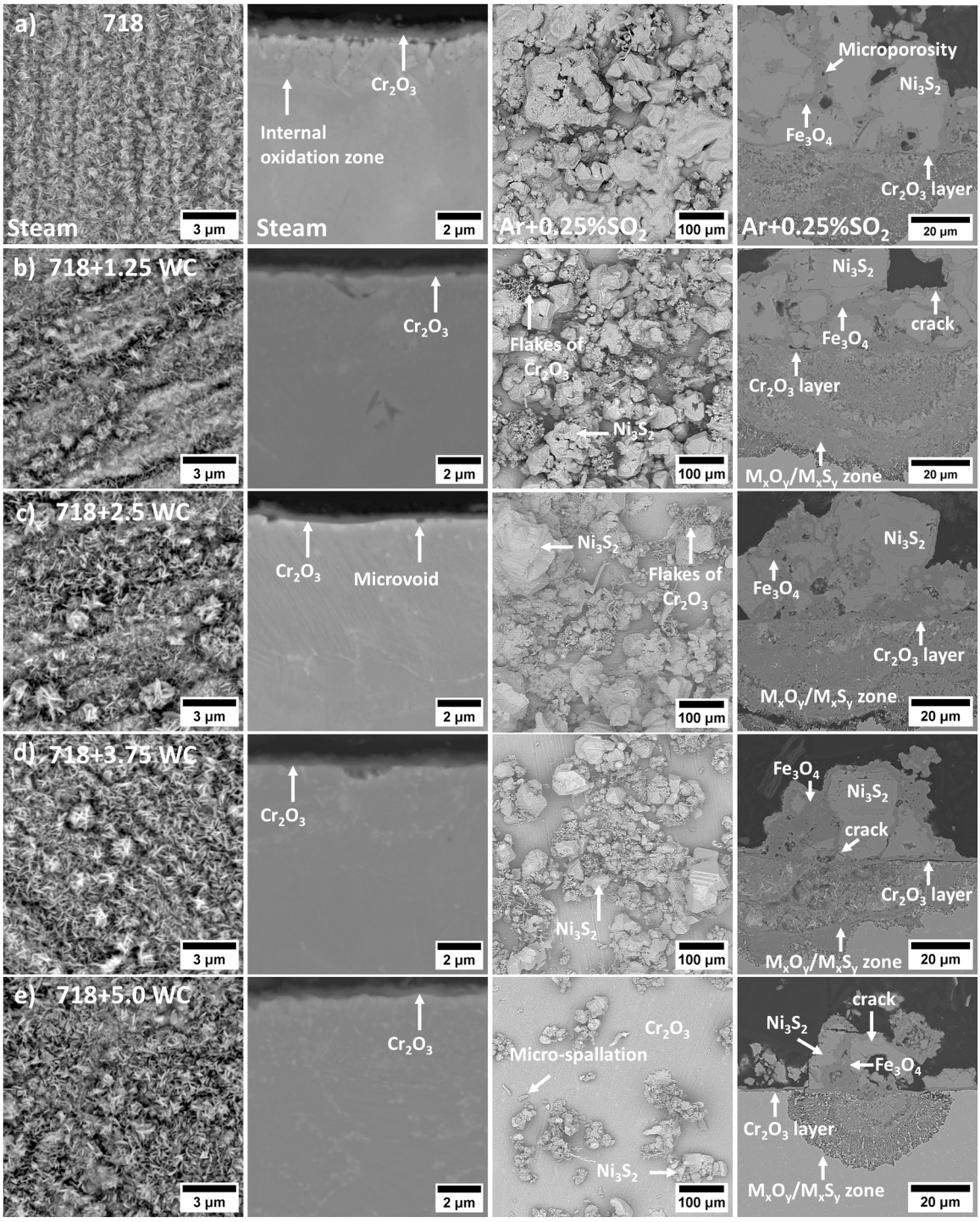

Fig. 13. SEM micrographs showing the morphology of oxide scales formed on Alloy 718 containing different WC NPs contents after 1000 h exposure at 704 °C: a) 0; b) 1.25%; c) 2.5%; d) 3.75%; e) 5.0% WC. The left column corresponds to steam oxidation, and the right column to oxidation in an Ar+ 0.25% SO_2 atmosphere.

gradual decrease in mass loss is observed, reaching approximately 0.059 mg/Nm in the variant with the highest NPs content. This also translates into a reduction in the wear coefficient from 3.70×10^{-8} mg/Nm for the 2.5% WC addition to approximately 2.92×10^{-8} mg/Nm in the last analyzed variant. Based on these measurements and earlier microstructural and X-ray diffraction studies, it can be assumed that improved tribological properties are largely due to the presence of hard, fine MC carbides in the interdendritic spaces. The carbides' crystallographic relationship with the matrix and their favourable morphology, specifically, the lack of agglomerates or clusters at grain boundaries, ensure good anchoring in the γ matrix. This favours uniform wear behaviour at the microscale and eliminates the risk of encountering weakened material fragments where carbide clusters are loosely bonded. Similar improvements in the wear resistance of Ni-based alloys from WC addition have been reported in the literature. Xia et al. [70] studied composites with 16 wt% of either fine or coarse WC particles. The materials were deposited by circular oscillating laser cladding. Their work demonstrated that a uniform distribution of WC particles enhances both grain-boundary strengthening and dispersion strengthening in the GH3536 Ni-based superalloy matrix. Fine WC particles were

Table 5
Hardness and dry-sliding test results of Alloy 718 modified with WC-NPs.

WC addition to Alloy 718, %wt	Hardness, HV10	Mass loss, %	Wear rate x10^{-8}, mg/Nm	R_z, μm	R_a, μm	S_a, μm
0	198 (±4)	0.090	4.56	9.72 (±0.73)	1.68 (±0.13)	1.74 (±0.07)
1.25	200 (±6)	0.089	4.55	9.01 (±1.00)	1.63 (±0.11)	1.61 (±0.13)
2.5	205 (±7)	0.076	3.70	8.52 (±1.15)	1.44 (±0.21)	1.47 (±0.11)
3.75	210 (±3)	0.069	3.52	8.21 (±1.31)	1.42 (±0.26)	1.43 (±0.12)
5.0	221 (±8)	0.059	2.92	7.27 (±1.18)	1.25 (±0.19)	1.29 (±0.09)

more effective than coarse ones in refining the matrix grain structure. This resulted in higher hardness and improved wear resistance. Leech et al. [71] likewise concluded that excellent resistance to abrasive wear is achieved at high WC contents. This occurs provided that the reinforcement is uniformly dispersed within the composite. At lower WC contents, the increased mean free path, which is the distance between reinforcing particles, facilitates deeper penetration of abrasive particles into the softer Ni-based matrix. This intensifies material removal and promotes WC particle pull-out. In contrast, a high WC content reduces the mean free path. This limits abrasive penetration and slows matrix degradation. Zhang et al. [72] explained the hardness enhancement in Ni-based alloy+WC composites through three principal mechanisms. First, decomposition of WC enables partial dissolution of W and C atoms into the alloy matrix. This results in lattice distortions that impede dislocation slip and contribute to solid-solution strengthening. Second, some of these atoms react with elements in the Ni-based matrix to form fine, hard, and thermodynamically stable carbides. These carbides act as obstacles to dislocation slip, thereby providing dispersion strengthening. Third, WC particles promote heterogeneous nucleation during solidification. This increases nucleation density, leading to grain refinement. The refined grain structure increases the grain-boundary area and resistance to deformation, resulting in fine-grain strengthening. Each of these mechanisms can therefore be identified in the Alloy 718 +WC composites processed by suction casting in the present work.

To gain insight into the prevailing wear mechanisms, the worn surfaces after dry-sliding tests were examined (Fig. 14). The reference alloy exhibits regions of intense plastic deformation accompanied by matrix material flow, while relatively few areas display wear features typical of abrasive wear, such as distinct scratches or grooves. Accumulations of oxides are observed on surface asperities and at the boundaries of smeared matrix regions. In contrast, the composite surfaces are comparatively smoother and characterised by narrower wear grooves, particularly evident in the specimen containing 5.0% WC. During sliding, the samples remain in contact with the abrasive ring, and the applied load induces plastic flow at the surface, leading to adhesive interactions. The WC-containing specimens exhibit slightly reduced surface damage. Consistent with earlier observations, their higher hardness limits abrasive ploughing, resulting in finer grooves and a more uniform worn surface. Dispersed hard precipitates gradually emerge at the surface during the early stages of wear, suppressing further adhesive and abrasive damage. During the initial run-in stage, abrasion is the dominant wear mechanism, and traces of this process remain visible on worn surfaces in regions of exposed matrix. Exposed areas of the Ni-based matrix are accompanied by fine oxide clusters, composed predominantly of iron oxides, along with locally Ni-enriched regions. In specimens containing 3.75% and 5.0% WC, fewer regions with transferred iron are observed, as the higher volume fraction of reinforcing particles reduces the area of direct contact between the composite matrix and the counterbody. Regions containing transferred iron are particularly prone to oxidation in ambient air, forming Fe-rich oxides with poor adhesion to the substrate, which tend to spall and migrate across the surface toward depressions or the edges of smeared matrix regions. Adhesively transferred iron from the counterbody is smeared over the samples' surface within the contact zone, however, this effect is limited by protruding strengthening precipitates. As dry sliding progresses, the temperature at the tribological contact increases, and oxidation becomes the dominant wear mechanism due to iron transferred from the counterbody. These oxides are prone to fragmentation and transport along the sliding direction, aided by the rotational motion of the counterbody, which partially facilitates the removal of detached oxide debris from the contact zone. The adhesively transferred Fe deposits are repeatedly deformed under contact pressure and evolving surface topography, thereby promoting the initiation of fatigue cracks that typically propagate transverse to the sliding direction. The relatively smooth topography observed in the contact region indicates that Fe transfer to the specimen surface, combined with the poor mechanical integrity of iron oxides, contributes to the formation of a low-roughness surface. Continuous oxidation, together with chipping and rapid oxide removal, maintains this smoothed condition. Surface changes were quantitatively characterised using the roughness parameters Rz, Ra, and Sa, all of which decrease with increasing WC content, consistent with the observed improvement in wear resistance. These findings, together with mass-loss measurements, confirm the anticipated beneficial effect of WC addition on the wear resistance of Alloy 718.

4. Conclusions

In this study, we investigated the relationship between microstructure and selected properties of the WC NPs- modified Alloy 718. The main conclusions can be drawn:

- The as-cast microstructure of all Alloy 718 +WC variants was clearly inhomogeneous due to the severe elemental segregation that occurs during solidification. Elements such as W and Fe preferentially partition to the dendritic core, while Nb and Mo preferentially partition to the interdendritic regions.
- WC nanoprecipitates were partially dissolved into the Alloy 718 matrix, significantly reducing the volume fraction of the detrimental Laves phase. Consequently, a higher fraction of complex (Nb,Mo,W)C carbides was formed. The dissolved WC acted as a reservoir of W and C, thereby affecting both the chemical composition and lattice parameters of the γ matrix and the MC carbides.
- -SEM and EBSD results indicate that, with increasing WC content in Alloy 718, the phase composition and precipitate volume fraction change. However, precipitate morphology remains largely unaffected. In the interdendritic regions, fine MC carbides and Laves phase were predominantly observed. This feature enhances fracture toughness.
- -A compact Cr_2O_3 layer provides excellent protection against steam oxidation for Alloy 718 + WC composites at 704 °C. Increasing WC content leads to a marked reduction in mass gain. Values drop below 0.059 mg/cm^2 after 1000 h.
- -Corrosion products from exposure to an Ar + 0.25% SO_2 gas mixture include Cr_2O_3, Fe_3O_4, and Ni_3S_2. This is observed regardless of the initial WC addition to the powder feedstock. WC-modified variants showed substantially lower mass increases. This was mainly due to the reduced amount of deleterious nickel sulfides forming on the external surface.
- -WC addition to Alloy 718 improves hardness and dry-sliding wear resistance. Exposure of hard carbides limits adhesive and abrasive wear. This leads to lower mass loss and lower surface roughness.

Ethical approval

This article does not contain any studies with human participants or

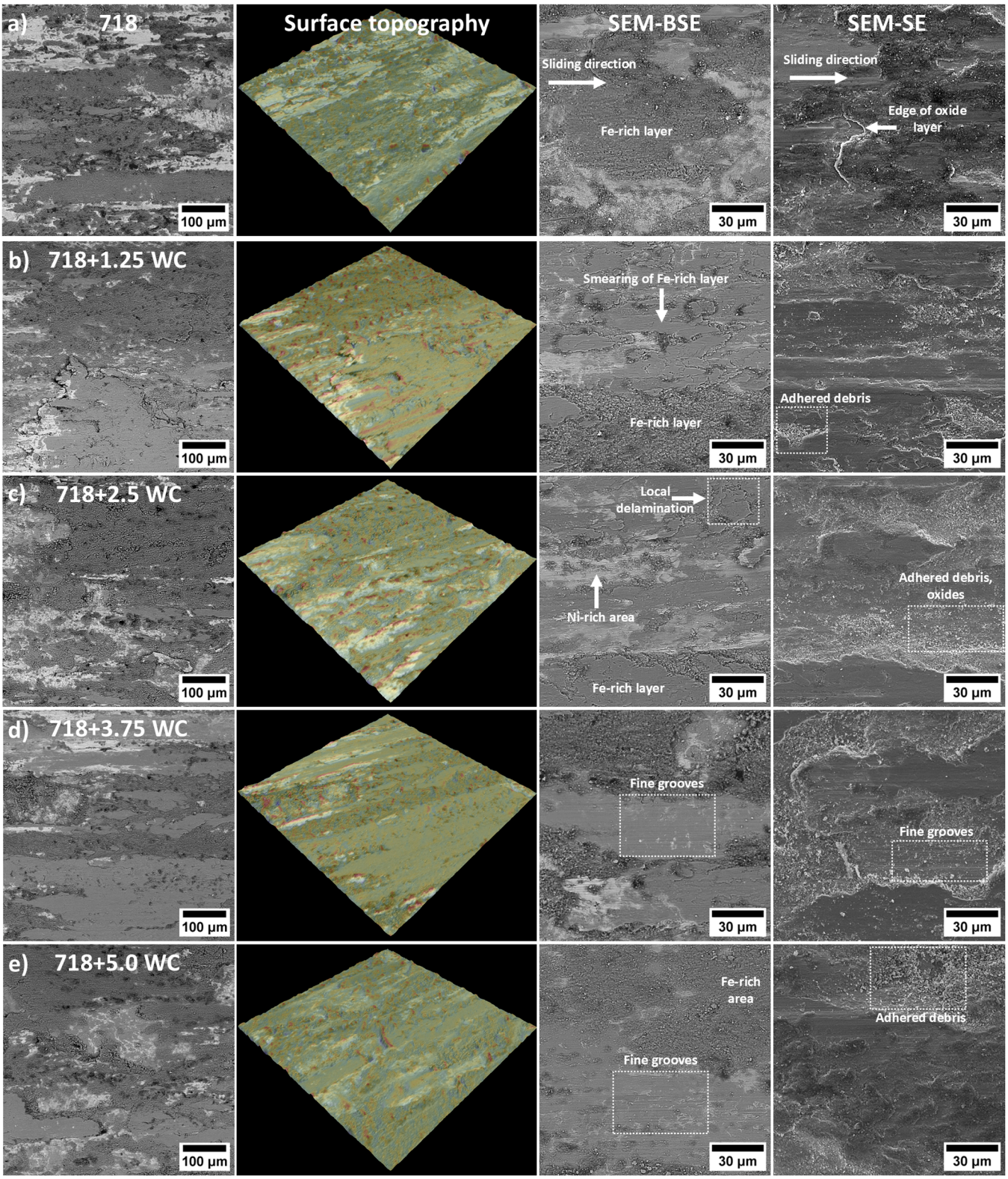

Fig. 14. Worn surface morphologies of Alloy 718 +WC composites following dry-sliding wear testing: a) 0; b) 1.25%; c) 2.5%; d) 3.75%; e) 5.0% WC.

animals performed by any of the authors.

CRediT authorship contribution statement

Tomasz Dudziak: Writing – review & editing, Investigation. **Tomasz Kargul:** Writing – review & editing, Investigation. **Norbert Schell:** Investigation. **Małgorzata Grudzień-Rakoczy:** Investigation. **Shigenari Hayashi:** Writing – review & editing, Supervision. **Robert Chulist:** Investigation. **Rakoczy Lukasz:** Writing – original draft, Visualization, Validation, Software, Resources, Project administration, Methodology, Investigation, Funding acquisition, Formal analysis, Data curation, Conceptualization. **Grzegorz Cios:** Writing – review & editing,

Investigation. **Rafał Cygan:** Writing – review & editing, Supervision. **Grzegorz Cempura:** Investigation. **Marcin Madej:** Writing – review & editing, Investigation. **Dawid Kozień:** Investigation. **Ewa Rząd:** Investigation.

Declaration of competing interest

The authors declare that they have no known competing financial interests or personal relationships that could have appeared to influence the work reported in this paper.

Acknowledgements

The author gratefully acknowledges the funding by National Center for Research and Development, Poland, under grant LIDER XIII – Development of the manufacturing and deposition technology of metal-ceramic nanocomposite coatings for the structural reconstruction of heat-resistant nickel-based superalloys (Project no. 0036/L-13/2022). ŁR would like to thank you to IDUB-Excellence Initiative – Research University (D10-ID 13464) for supporting a cooperation between AGH University of Kraków and Hokkaido University (Japan).

Data availability

Related research data is available on demand from the corresponding author.

References

[1] G. Gudivada, A.K. Pandey, Recent developments in nickel-based superalloys for gas turbine applications: Review, J. Alloy. Compd. 963 (2023) 171128, https://doi.org/10.1016/j.jallcom.2023.171128.
[2] Y. Chen, Z. Yao, H. Wang, J. Dong, J. Peng, M. Ren, H. Yang, L. Leng, Damage mechanism on superalloy surface of coated gas turbine vanes after long-term service, Eng. Fail. Anal. 179 (2025) 109797, https://doi.org/10.1016/j.engfailanal.2025.109797.
[3] A.H. Jafarzadeh, M.S. Shahriari, R. Ashiri, Effects of GTAW process and post-welding heat treatment on the microstructure evolution, cracking behavior and hardness of Inconel 939 superalloy using Inconel 617 filler metal, J. Mater. Res. Technol. 38 (2025) 1782–1791, https://doi.org/10.1016/j.jmrt.2025.08.040.
[4] D. Wang, Z. Liu, G. Deng, X. Zhou, S. Li, H. Wang, Y. Yang, C. Han, A laser powder bed fusion–based methodology for repairing damaged nickel-based turbine blades: Investigation of interfacial characteristics and hot isostatic pressing treatment, Mater. Charact. 212 (2024) 113948, https://doi.org/10.1016/j.matchar.2024.113948.
[5] H.S. Kang, M. Gwak, B.J. Kim, K. Park, Y. Son, S.M. Seo, S. Kim, H. Lee, J.G. Kim, Mater. Sci. Eng. A 913 (2024) 147083, https://doi.org/10.1016/j.msea.2024.147083.
[6] A. Ariaseta, F. Hanning, J. Andersson, O. Ojo, Hot ductility behavior of new Ni-based superalloy G27: Influence of solution annealing on the liquation cracking susceptibility, J. Mater. Res. Technol. 38 (2025) 4133–4149, https://doi.org/10.1016/j.jmrt.2025.08.241.
[7] A. Kruk, G. Cempura, Decomposition of the Laves phase in the fusion zone of the Inconel 718/ATI 718Plus® welded joint during isothermal holding at a temperature of 649 °C, Mater. Charact. 196 (2023) 112560, https://doi.org/10.1016/j.matchar.2022.112560.
[8] Y. Liu, W. Liu, H. Fan, Q. Zhang, Y. Ma, F. Wang, H. Zhang, Role of nano-TiC particles in enhancing the microstructure and wear resistance of IN718 superalloys fabricated by directed energy deposition, Ceram. Int. 51 (2025) 46944, https://doi.org/10.1016/j.ceramint.2025.07.398.
[9] A. Graboś, P. Rutkowski, J. Huebner, D. Kozień, S. Zhang, Y.-L. Kuo, D. Kata, S. Hayashi, Oxidation performance of spark plasma sintered Inconel 625–NbC metal matrix composites, Corros. Sci. 205 (2022) 110453, https://doi.org/10.1016/j.corsci.2022.110453.
[10] G. Ghosh, S. Agrawal, A. Saigal, R. Singh, Effect of process parameters on the porosity in laser-directed energy deposition of Al_2O_3 reinforced Inconel-based composite coating, Manuf. Lett. 35 (2023) 683–688, https://doi.org/10.1016/j.mfglet.2023.08.078.
[11] L. Li, T. Dong, C. Guo, F. Jiang, Z. Shen, Y. Liu, M. Diao, H. Song, Effect of core–shell structure formed by Y_2O_3-doping on cracking inhibition in SLMed Y_2O_3/Mar-M247 alloy, Compos. Part A 195 (2025) 108981, https://doi.org/10.1016/j.compositesa.2025.108981.
[12] Z. Zhang, Q. Han, Z. Liu, X. Wang, L. Wang, X. Yang, T. Ma, Z. Gao, Influence of the TiB_2 content on the processability, microstructure and high-temperature tensile performance of a Ni-based superalloy by laser powder bed fusion, J. Alloy. Compd. 908 (2022) 164656, https://doi.org/10.1016/j.jallcom.2022.164656.
[13] N. Hassan, M. Kim, S. Shin, J. Park, U. Kim, Y. Kim, S. Kim, S.-S. Ryu, Y. Kwak, J. Cho, WC-reinforced AlN–Y_2O_3 composites: Grain coarsening for toughness and thermal performance, J. Alloy. Compd. 1044 (2025) 184534, https://doi.org/10.1016/j.jallcom.2025.184534.
[14] H. Wang, K. Liu, J. Li, S.N. Geng, L. Jing, V. Skuratov, Reinforcements/matrix microinterface evolution and properties of in-situ Ni60A/WC coatings prepared by laser cladding, Surf. Coat. Technol. 484 (2024) 130834.
[15] W.Q. Sun, D.Q. Zhang, X. Chen, K.Y. Wang, J.Q. Zhang, Y.J. Jia, Effect of the scanning speed of laser cladding on microstructure and mechanical properties of WC/Ni composite coatings, J. Mech. Sci. Technol. 36 (2022) 679–687.
[16] H. Zhang, Y. Wu, Y. Wang, W. Deng, G. Xu, K. Luo, In-situ nanoscale precipitation behavior and strengthening mechanism of WC/IN718 composites manufactured by laser powder bed fusion, Compos. Part B 284 (2024) 111727, https://doi.org/10.1016/j.compositesb.2024.111727.
[17] Y. Gao, H. Chen, J. Zhou, W. Tian, H. Nie, W. Wang, Microstructures and wear behaviors of WC particle reinforced Ni-based composites fabricated by selective laser melting, J. Manuf. Process 95 (2023) 291–301, https://doi.org/10.1016/j.jmapro.2023.03.075.
[18] H. Wang, K. Liu, J. Li, S. Geng, L. Jing, V. Skuratov, Reinforcements/matrix micro-interface evolution and properties of in-situ Ni60A/WC coatings prepared by laser cladding, Surf. Coat. Technol. 484 (2024) 130834, https://doi.org/10.1016/j.surfcoat.2024.130834.
[19] L. Xu, L. Zhu, M. Yu, J. Ning, Z. Yang, Z. Jiang, Microstructure and wear performance of Inconel 718 composite coatings reinforced with multi-size and content WC–Co fabricated by laser cladding, J. Therm. Spray. Technol. 34 (2025) 337–353, https://doi.org/10.1007/s11666-024-01908-y.
[20] D. Deschuyteneer, F. Pettit, M. Gonon, F. Cambier, Surf. Coat. Technol. 311 (2017) 365–373, https://doi.org/10.1016/j.surfcoat.2016.12.110.
[21] A. Garcia, M.R. Fernandez, J.M. Cuetos, R. Gonzalez, A. Ortiz, M. Cadenas, Study of the sliding wear and friction behavior of WC + NiCrBSi laser cladding coatings as a function of actual concentration of WC reinforcement particles in ball-on-disk test, Tribol. Lett. 63 (2016) 1–10, https://doi.org/10.1007/s11249-016-0734-3.
[22] C.P. Paul, S.K. Mishra, P. Tiwari, L.M. Kukreja, Solid-particle erosion behaviour of WC/Ni composite clad layers with different contents of WC particles, Opt. Laser Technol. 50 (2013) 155–162.
[23] Z.H. Tian, Y.T. Zhao, Y.J. Jiang, H.P. Ren, Microstructure and properties of Inconel 625 + WC composite coatings prepared by laser cladding, Rare Met 40 (2021) 2281–2291, https://doi.org/10.1007/s12598-020-01507-0.
[24] Z. Liu, J. Cabrero, S. Niang, Z. Al-Taha, Improving corrosion and wear performance of HVOF-sprayed Inconel 625 and WC–Inconel 625 coatings by high power diode laser treatments, Surf. Coat. Technol. 201 (2007) 7149–7158, https://doi.org/10.1016/j.surfcoat.2007.01.032.
[25] T.E. Abioye, P.K. Farayibi, D.G. McCartney, A.T. Clare, Effect of carbide dissolution on the corrosion performance of tungsten carbide reinforced Inconel 625 wire laser coating, J. Mater. Process. Technol. 231 (2016) 89–99, https://doi.org/10.1016/j.jmatprotec.2015.12.023.
[26] G. Ertugrul, A. Emdadi, A. Jedynak, S. Weiß, S. Hartel, Hot forming behavior of tungsten carbide reinforced Ni-based superalloy 625 additively manufactured by laser directed energy deposition, Addit. Manuf. Lett. 13 (2025) 100267, https://doi.org/10.1016/j.addlet.2025.100267.
[27] Y. Liu, X. Zheng, H. Shen, G. Chang, Z. Zhang, Z. Zhang, C. Yuan, W. Wang, N. Li, W. Zhang, Microstructure evolution of γ′-strengthened binder phase and corrosion behavior in WC–superalloy model hard materials, J. Alloy. Compd. 1039 (2025) 183170, https://doi.org/10.1016/j.jallcom.2025.183170.
[28] M. Rzeszotarska, I. Kunce, D. Zasada, M. Polański, Feasibility study of metal matrix composite (In625–WC) manufacturing by laser engineered net shaping (LENS®), Arch. Metall. Mater. 69 (2024) 1675–1683, https://doi.org/10.24425/amm.2024.152097.
[29] T. Kozieł, K. Pajor, Ł. Gondek, Cooling rate evaluation during solidification in the suction casting process, J. Mater. Res. Technol. 9 (2020) 13502–13508, https://doi.org/10.1016/j.jmrt.2020.09.082.
[30] A. Wójcik, R. Chulist, A. Szewczyk, B. Morończyk, Ł. Żrodowski, R. Wróblewski, M. Kowalczyk, A. Kolano-Burian, P. Zackiewicz, N. Schell, W. Maziarz, Microstructure and texture control of Ni–Mn–Ga magnetic shape memory alloys manufactured by laser powder bed fusion, Addit. Manuf. 86 (2024) 104225, https://doi.org/10.1016/j.addma.2024.104225.
[31] R. Chulist, A. Wójcik, A. Sozinov, T. Tokarski, M. Faryna, N. Schell, W. Skrotzki, B. Li, H. Sehitoglu, X. Li, W. Maziarz, Adaptive phase or variant formation at the austenite/twinned martensite interface in modulated Ni–Mn–Ga martensite, Adv. Funct. Mater. 34 (2024) 2307322, https://doi.org/10.1002/adfm.202307322.
[32] F. Kateusz, A. Polkowska, K. Chat-Wilk, K. Chrzan, D. Serafin, S. Pawlik, T. Dudziak, J. Jedliński, Steam oxidation of thermally deposited coatings from 304L and recycled 316L/Z100 steels: Influence of temperature, coatings microstructure and steel recycling, Surf. Coat. Technol. 494 (2024) 131478, https://doi.org/10.1016/j.surfcoat.2024.131478.
[33] Ł. Rakoczy, M. Grudzień-Rakoczy, G. Cempura, T. Kargul, E. Rząd, M. Madej, A. Kruk, T. Dudziak, D. Kozień, R. Cygan, R. Chulist, D. Galusek, Microstructure, phase transformation temperatures and long-term stability of ex-situ Alloy 718 + TiB_2 metal–ceramic nanocomposites as repair coatings for aerospace applications, Sci. Rep. 16 (2026) 95, https://doi.org/10.1038/s41598-025-29049-4.
[34] ASTM G77 standard - Standard Test Method for Ranking Resistance of Materials to Sliding Wear Using Block-on-Ring Wear Test.
[35] K. Kulawik, P.A. Buffat, A. Kruk, A.M. Wusatowska-Sarnek, A. Czyrska-Filemonowicz, Imaging and characterization of γ′ and γ″ nanoparticles in Inconel 718 by EDX elemental mapping and FIB–SEM tomography, Mater. Charact. 100 (2015) 74–80, https://doi.org/10.1016/j.matchar.2014.12.012.

[36] Ł. Rakoczy, M. Grudzień-Rakoczy, B. Rutkowski, R. Cygan, F. Hanning, G. Cios, S. Habisch, J. Andersson, P. Mayr, A. Zielińska-Lipiec, The role of the strengthening phases on the HAZ liquation cracking in a cast Ni-based superalloy used in industrial gas turbines, Arch. Civ. Mech. Eng. 23 (2023) 119, https://doi.org/10.1007/s43452-023-00659-x.
[37] W.D. Cao, R.L. Kennedy, M.P. Willis, in: E.A. Loria (Ed.), in: Superalloys 1991, TMS, Warrendale, PA, 1991, pp. 147–160, https://doi.org/10.7449/1991/superalloys_1991_147_160.
[38] M.J. Sohrabi, H. Mirzadeh, M. Rafiei, Solidification behavior and Laves phase dissolution during homogenization heat treatment of Inconel 718 superalloy, Vacuum 154 (2018) 235–243, https://doi.org/10.1016/j.vacuum.2018.05.019.
[39] S. He, S. Park, D. Shim, C. Yao, W. Zhang, Study on microstructure and abrasive behaviors of Inconel 718–WC composite coating fabricated by laser directed energy deposition, J. Mater. Res. Technol. 21 (2022) 2926–2946, https://doi.org/10.1016/j.jmrt.2022.10.088.
[40] S. He, S. Park, D. Shim, C. Yao, M. Li, S. Wang, Effect of substrate preheating on the microstructure and bending behavior of WC–Inconel 718 composite coating synthesized via laser directed energy deposition, Int. J. Refract. Met. Hard Mater. 115 (2023) 106299, https://doi.org/10.1016/j.ijrmhm.2023.106299.
[41] G.A. Knorovsky, M.J. Cieslak, T.J. Headley, A.H. Romig, W.F. Hammetter, Inconel 718: A solidification diagram, Metall. Trans. A 20 (1989) 2149–2158, https://doi.org/10.1007/BF02650300.
[42] M.J. Cieslak, T.J. Headley, T. Kollie, A.D. Romig, Jr., A melting and solidification study of alloy 625, Metall. Trans. A 19 (1988) 2319–2333, https://doi.org/10.1007/BF02645056.
[43] M.S.A. Karunaratne, S. Kyaw, A. Jones, R. Morell, R.C. Thomson, Modelling the coefficient of thermal expansion in Ni-based superalloys and bond coatings, J. Mater. Sci. 51 (2016) 4213–4226, https://doi.org/10.1007/s10853-015-9554-3.
[44] S. Kobayashi, Solute redistribution during solidification with diffusion in solid phase: A theoretical analysis, J. Cryst. Growth 88 (1988) 1–8.
[45] H.M. Wang, J.H. Zhang, Y.J. Tang, Z.Q. Hu, N. Yukawa, M. Morinaga, Y. Murata, Rapidly solidified MC carbide morphologies of a laser-glazed single-crystal nickel-base superalloy, Mater. Sci. Eng. A 156 (1) (1992) 109–116, https://doi.org/10.1016/0921-5093(92)90421-v.
[46] S. Sui, J. Chen, R. Zhang, X. Ming, F. Liu, X. Lin, Tensile deformation behavior of laser repaired Inconel 718 with a non-uniform microstructure, Mater. Sci. Eng. A 688 (2017) 480–487, https://doi.org/10.1016/j.msea.2017.01.110.
[47] B. Tang, Y. Tan, T. Xu, Z. Sun, X. Li, Effects of TiB_2 particle content on microstructure, mechanical properties and tribological properties of Ni-based composite coatings reinforced with TiB_2 particles by laser cladding, Coatings 10 (2020) 813, https://doi.org/10.3390/coatings10090813.
[48] C. Kumara, A.R. Balachandramurthi, S. Goel, F. Hanning, J. Moverare, Toward a better understanding of phase transformations in additive manufacturing of Alloy 718, Materialia 13 (2020) 100862, https://doi.org/10.1016/j.mtla.2020.100862.
[49] P. Mohammadpour, H. Yuan, A.B. Phillion, Microstructure evolution of Inconel 625 alloy during single-track laser powder bed fusion, Addit. Manuf. 55 (2022) 102824, https://doi.org/10.1016/j.addma.2022.102824.
[50] P. Vespa, P.T. Pinard, R. Gauvin, M. Brochu, Analysis of WC/Ni-based coatings deposited by controlled short-circuit MIG welding, J. Mater. Eng. Perform. 21 (2012) 865–876, https://doi.org/10.1007/s11665-011-9947-7.
[51] C. Pan, D. Zhu, H. Luo, K. Kosiba, S. Qu, C. Yang, X. Li, Fabrication of high-performance CoCrNi medium entropy alloy by laser powder bed fusion, Eff. grain Bound. Segreg. Compos. Part B 253 (2023) 110540, https://doi.org/10.1016/j.compositesb.2023.110540.
[52] N.N. Stepanova, D.P. Rodionov, V.A. Sazonova, E.N. Khlystov, Structure formation in ⟨001⟩ single crystals of a nickel-based superalloy solidified with TiCN powder addition, Mater. Sci. Eng. A 284 (2000) 88–92, https://doi.org/10.1016/S0921-5093(00)00763-2.
[53] H. Cai, J. Hou, Y.-A. Guo, J. Xing, L.-Z. Zhou, The evolution of carbides during long-term creep/aging of nickel-based superalloy K444, J. Mater. Res. Technol. 28 (2024) 3631–3640, https://doi.org/10.1016/j.jmrt.2023.12.236.
[54] C. Zhang, L. Zhang, Y. Wang, S. Li, J. Li, Z. Xie, Microstructural evolution and dissolution mechanisms of hard WC particles reinforced nickel-based composite coatings fabricated by plasma transferred arc welding, J. Alloy. Compd. 1019 (2025) 179293, https://doi.org/10.1016/j.jallcom.2025.179293.
[55] Q. Tan, Y. Yin, A. Prasad, G. Li, Q. Zhu, D.H. StJohn, M.-X. Zhang, Demonstrating the roles of solute and nucleant in grain refinement of additively manufactured aluminium alloys, Addit. Manuf. 49 (2022) 102516, https://doi.org/10.1016/j.addma.2021.102516.
[56] Y. Zhao, T. Ma, Z. Gao, Y. Feng, C. Li, Q. Guo, Z. Ma, Y. Liu, Significant reduction of grain size and texture intensity in laser powder bed fusion fabricated nickel-based superalloy by increasing constitutional supercooling, Compos. Part B 266 (2023) 111040, https://doi.org/10.1016/j.compositesb.2023.111040.
[57] M. Volmer, Über Keimbildung und Keimwirkung als Spezialfälle der heterogenen Katalyse, Z. Elektrochem. Angew. Phys. Chem. 35 (1929) 555–561.
[58] J.C. Yang, E. Schumann, I. Levin, M. Rühle, Transient oxidation of NiAl, Acta Mater. 46 (1998) 2195–2201, https://doi.org/10.1016/S1359-6454(97)00378-9.
[59] G.R. Belton, R.L. McCarron, The volatilization of tungsten in the presence of water vapor, J. Phys. Chem. 68 (1964) 1852–1856, https://doi.org/10.1021/j100789a030.
[60] F.H. Latief, N.H. Alrasheedi, Anisotropic oxidation resistance in a Ni-base single crystal superalloy, Int. J. Electrochem. Sci. 10 (2015) 2183–2193.
[61] D. Kim, J.-H. Chang, J. Park, J.J. Pak, Formation and behavior of Kirkendall voids within intermetallic layers of solder joints, J. Mater. Sci. Mater. Electron 22 (2011) 703–716, https://doi.org/10.1007/s10854-011-0357-2.
[62] A. Vesel, M. Mozetic, M. Balat-Pichelin, Sequential oxidation and reduction of tungsten/tungsten oxide, Thin Solid Films 591 (2015) 174–181, https://doi.org/10.1016/j.tsf.2015.02.019.
[63] A. Yamauchi, K. Kurokawa, H. Takahashi, Evaporation of Cr_2O_3 in atmospheres containing H_2O, Oxid. Met. 59 (2003) 517–527, https://doi.org/10.1023/A:1023671206976.
[64] I. Dainezi, B. Gleeson, B.R. Buzatti, A.M. de Sousa Malafaia, C.A.D. Rovere, TiNbCr multi-principal element alloy oxidation behavior in air at 800–1000 °C, High. Temp. Corros. Mater. 101 (2024) 789–810, https://doi.org/10.1007/s11085-024-10246-x.
[65] H.J.T. Ellingham, Reducibility of oxides and sulphides in metallurgical processes, J. Soc. Chem. Ind. 63 (1944) 125–160, https://doi.org/10.1002/jctb.5000630501.
[66] D.J. Young, High Temperature Oxidation and Corrosion of Metals, 2nd ed., 8, Elsevier, Amsterdam, 2016 https://doi.org/10.1016/C2014-0-00259-6.
[67] J.D. Christian, W.P. Gilbreath, Defect structure of NiO and rates and mechanisms of formation from atomic oxygen and nickel, Oxid. Met. 9 (1975) 1–25, https://doi.org/10.1007/BF00613490.
[68] X. Montero, A. Ishida, T.M. Meißner, H. Murakami, M.C. Galetz, Effect of surface treatment and crystal orientation on hot corrosion of a Ni-based single-crystal superalloy, Corros. Sci. 166 (2020) 108472, https://doi.org/10.1016/j.corsci.2020.108472.
[69] P. Liu, J.A. Rodriguez, Interaction of sulfur dioxide with titanium–carbide nanoparticles and surfaces: A density functional study, J. Chem. Phys. 119 (2003) 10895–10903, https://doi.org/10.1063/1.1619945.
[70] Y. Xia, H. Chen, X. Liang, J. Lei, Circular oscillating laser melting deposition of nickel-based superalloy reinforced by WC: Microstructure, wear resistance and electrochemical properties, J. Manuf. Process 68 (2021) 1694–1704, https://doi.org/10.1016/j.jmapro.2021.06.074.
[71] P.W. Leech, X.S. Li, N. Alam, Comparison of abrasive wear of a complex high alloy hardfacing deposit and WC–Ni based metal matrix composite, Wear 294295 (2012) 380–386, https://doi.org/10.1016/j.wear.2012.07.015.
[72] K. Zhang, H. Ju, F. Xing, W. Wang, Q. Li, X. Yu, W. Liu, Microstructure and properties of composite coatings by laser cladding Inconel 625 reinforced with WC particles on non-magnetic steel, Opt. Laser Technol. 163 (2023) 109321, https://doi.org/10.1016/j.optlastec.2023.109321.